Applied Catalysis B: Environmental 318 (2022) 121836

Contents lists available at ScienceDirect

Applied Catalysis B: Environmental

journal homepage: www.elsevier.com/locate/apcatb

Enhancing CO_2 methanation over Ni catalysts supported on sol-gel derived Pr_2O_3-CeO_2: An experimental and theoretical investigation

Anastasios I. Tsiotsias [a], Nikolaos D. Charisiou [a], Eleana Harkou [b], Sanaa Hafeez [c], George Manos [c], Achilleas Constantinou [b,*], Aseel G.S. Hussien [d,e], Aasif A. Dabbawala [d,e], Victor Sebastian [f,g,h], Steven J. Hinder [i], Mark A. Baker [i], Kyriaki Polychronopoulou [d,e], Maria A. Goula [a,**]

[a] Laboratory of Alternative Fuels and Environmental Catalysis (LAFEC), Department of Chemical Engineering, University of Western Macedonia, GR-50100, Greece
[b] Department of Chemical Engineering, Cyprus University of Technology, 57 Corner of Athinon and Anexartisias, Limassol 3036, Cyprus
[c] Department of Chemical Engineering, University College London, London WCIE7JE, UK
[d] Department of Mechanical Engineering, Khalifa University of Science and Technology, P.O. Box 127788, Abu Dhabi, UAE
[e] Center for Catalysis and Separations, Khalifa University of Science and Technology, P.O. Box 127788, Abu Dhabi, UAE
[f] Department of Chemical Engineering and Environmental Technology, Universidad de Zaragoza, Campus Río Ebro-Edificio I+D, 50018 Zaragoza, Spain
[g] Instituto de Nanociencia y Materiales de Aragón (INMA), Universidad de Zaragoza, CSIC, c/ María de Luna 3, 50018 Zaragoza, Spain
[h] Networking Research Center on Bioengineering, Biomaterials and Nanomedicine, CIBERBBN, 28029 Madrid, Spain
[i] The Surface Analysis Laboratory, Faculty of Engineering and Physical Sciences, University of Surrey, Guildford GU2 4DL, UK

ARTICLE INFO

Keywords:
CO_2 methanation
Sol-gel synthesis
Metal dispersion
CFD modelling
Model validation

ABSTRACT

Ni-based catalysts supported on sol-gel prepared Pr-doped CeO_2 with varied porosity and nanostructure were tested for the CO_2 methanation reaction. It was found that the use of ethylene glycol in the absence of H_2O during a modified Pechini synthesis led to a metal oxide support with larger pore size and volume, which was conducive toward the deposition of medium-sized Ni nanoparticles confined into the nanoporous structure. The high Ni dispersion and availability of surface defects and basic sites acted to greatly improve the catalyst's activity. CFD simulations were used to theoretically predict the catalytic performance given the reactor geometry, whereas COMSOL and ASPEN software were employed to design the models. Both modelling approaches (CFD and process simulation) showed a good validation with the experimental results and therefore confirm their ability for applications related to the prediction of the CO_2 methanation behaviour.

1. Introduction

Following the industrial revolution, the sharp increase in anthropogenic CO_2 emissions has caused a great spike in its concentration in our atmosphere [1]. Since CO_2 acts as a greenhouse gas, it leads to increases in the global temperature, which disrupt the delicate balance of our planet's climate and ecosystems [1,2]. Capturing and converting part of this emitted CO_2 toward value-added products aims to mitigate the adverse effects of climate change, while transitioning toward a net-zero economy [2,3]. Moreover, captured CO_2 can also be converted via hydrogenation into high-energy density fuels/ energy carriers (e.g., methane, jet fuel), circumventing problems related with the storage and transportation of hydrogen, which has a very low volumetric energy density [4–7]. CO_2 hydrogenation to methane (i.e., CO_2 methanation or the Sabatier reaction) has also been indicated as potentially useful for Mars exploration missions, since abundant CO_2 from the Martian atmosphere can be used to generate fuel for methane-powered rocket engines [8]. The Sabatier process is an exothermic one and is described via the following equation (Eq. (1)):

$$CO_2 + 4\,H_2 \rightarrow CH_4 + 2\,H_2O \quad (1)$$

The CO_2 methanation catalysts studied until now mostly utilize Ni, Ru or Rh [8–11] as active metals. However, Ru and especially Rh are quite expensive (which inhibits large-scale industrial implementation)

* Correspondence to: Cyprus University of Technology, Department of Chemical Engineering, Limassol 3036, Cyprus.
** Correspondence to: University of Western Macedonia, Department of Chemical Engineering, Laboratory of Alternative Fuels and Environmental Catalysis, Koila, Kozani 50100, Greece.
E-mail addresses: a.konstantinou@cut.ac.cy (A. Constantinou), mgoula@uowm.gr (M.A. Goula).

https://doi.org/10.1016/j.apcatb.2022.121836
Received 13 May 2022; Received in revised form 15 July 2022; Accepted 9 August 2022
Available online 10 August 2022

and thus, Ni-based catalysts are much more often employed due to their high activity and low-cost [9,10,12]. The role of support in Ni-based catalysts is vital, as it can provide the active sites for CO_2 chemisorption/ activation and enhance the dispersion of the metallic Ni phase [13]. Ni/CeO_2-type catalysts are reported in numerous studies to be greatly superior to Ni catalysts supported on other metal oxides (e.g., Al_2O_3, SiO_2, TiO_2 or ZrO_2), especially in relation to low-temperature activity and CH_4 selectivity, as the oxygen lability of CeO_2 can promote the CO_2 chemisorption/ activation and the conversion/ removal of reaction intermediates [9–15]. Doping of the CeO_2 supports with aliovalent cations (e.g., Pr^{3+}, La^{3+} Gd^{3+}, Y^{3+}) has also been shown to further increase the oxygen mobility by increasing the population of oxygen vacancies [16–20]. To this end, low amounts of Pr-doping in Ni/CeO_2 has been shown to be particularly successful toward enhancing the CO_2 methanation activity, due to the redox activity of PrO_x and its high solubility in CeO_2 [16–18].

Another important factor that needs consideration is the architecture/ nanostructure of the CeO_2-based support [21–24]. Hashimoto et al. [21] showed that Ni supported on CeO_2 nanorods was significantly more active compared to Ni supported on other CeO_2 nanostructures (nanocubes and nanooctahedra), due to the higher activity of surface oxygen on the (110) facet of CeO_2. Du et al. [22] reported that Ni supported on CeO_2 nanoplates rich in oxygen vacancies provided a highly active CO_2 methanation catalyst. Hongmanorom et al. [23] employed a hard template synthesis method (nanocasting), to prepare ordered mesoporous CeO_2, followed by the deposition of Ni nanoparticles. Ni supported on ordered mesoporous CeO_2 was found to be greatly superior in catalytic activity compared to Ni supported on precipitated CeO_2. On the other hand, Cárdenas-Arenas et al. [24] found that Ni supported on CeO_2 with uncontrolled structure was more active than Ni supported on 3D ordered macroporous (3DOM) CeO_2, due to a less favourable Ni-CeO_2 contact and ratio between Ni-O-Ce and metallic Ni sites. In short, it can be deduced that the surface defect chemistry, the available surface area, but also the Ni dispersion and mean size of supported Ni nanoparticles are important parameters that affect the catalytic activity of Ni/CeO_2-type catalysts. However, none of the works mentioned above [21–24] employed doped/ modified CeO_2 supports, using unmodified CeO_2 instead.

In a previous work carried out by our group [16], we studied Ni-based CO_2 methanation catalysts supported on Mg-, Sm-, or Pr-doped CeO_2 and we were able to show that the Ni/Pr- CeO_2 catalyst exhibited a more active and stable performance in comparison with the rest of the samples. In a subsequent work [17], we examined the effect of the content of Pr in the CeO_2 support (prepared via citrate sol-gel) and we were able to establish that the optimum composition was Ni supported on 10 at% Pr-doped CeO_2 ($Ce_{0.9}Pr_{0.1}O_{2-\delta}$). However, the relatively mediocre Ni dispersion and low-temperature activity has led us to consider alternative synthesis methods for the Pr-doped CeO_2 support.

Thus, in this work, we used Pechini and modified Pechini sol-gel type synthesis methods with the aim of altering the porous architecture of the Pr-doped CeO_2 supports in Ni/Pr-CeO_2 CO_2 methanation catalysts and compared these with the performance of catalytic materials whose supports were synthesized with the typical citrate sol-gel synthesis. We note that the sol-gel type Pechini synthesis method, which relies on the polycondensation between a polyol (usually ethylene glycol) and metal-citrate complexes, is similar to citrate sol-gel, but offers more flexibility due to the ability to tune the final metal oxide structure via modifying the synthesis conditions and/ or choosing various polyols/ carboxylic acid molecules [25–27]. We were able to show, that the synthesis method affects the textural characteristics and Ni dispersion, greatly influencing the catalytic activity. In particular, the Ni catalyst supported on Pr-doped CeO_2 prepared with a modified, H_2O-free, Pechini method with ethylene glycol and citric acid (Ni/MPC), is shown to be the most active catalyst owing to its improved surface area, pore volume, surface basicity and Ni dispersion.

In addition, for the work reported herein, we decided to couple the experimental work with computational modelling, as numerical studies that use software, such as computational fluid dynamics (CFD) and process flowsheet simulation modelling can provide an excellent understanding of parameter optimisation [28–33]. We note that the available literature concerning experimental work coupled with computational modelling, regarding the CO_2 methanation reaction, is still scant [34–40].

2. Experimental part

2.1. Preparation methods

Pr-doped CeO_2 oxide supports (10 mol% Pr or $Ce_{0.9}Pr_{0.1}O_{2-\delta}$ nominal composition) were prepared via different sol-gel-type methods:

For the citrate sol-gel synthesis (CSG), initially $Ce(NO_3)_3{\cdot}6H_2O$ (Sigma-Aldrich, 99%) along with $Pr(NO_3)_3{\cdot}6H_2O$ (Sigma-Aldrich, 99.9%) in calculated amounts were added in 100 ml d-H_2O. This was followed by the addition of citric acid (Fluka, 99.5%) (1.5:1 molar ratio of citric acid: total metal cations). The temperature was then increased to 80 ^oC for the solvent evaporation, which eventually led to the emergence of a viscous and greenish gel-like syrup. After drying at 130 ^oC overnight, the dried gel was homogenized and calcined at 400 ^oC for 1 h and then at 500 ^oC for 4 h. A CeO_2 ($CeO_{2-\delta}$) reference was also prepared via this method.

For the Pechini synthesis (PC), a similar procedure to citrate sol-gel was followed, with the only difference being the addition of ethylene glycol (Sigma-Aldrich, 99.8%) along with citric acid in a molar ratio of ethylene glycol to citric acid to total metals of 3:1.5:1. This led to a more compact polymer gel after the drying step.

For the modified Pechini synthesis (MPC), citric acid and the metal nitrates were directly dissolved in ethylene glycol in the absence of water. The amount of ethylene glycol was increased, so that the molar ratio of ethylene glycol to citric acid to total metal cations was equal to 15:1.5:1. Citric acid was first dissolved in ethylene glycol at 60 ^oC, followed by stirring for 1 h. The metal nitrates of Ce and Pr were then added at 30 min intervals and then left stirring at 60 ^oC for 2 h. Afterwards, the temperature was increased to 130 ^oC and the mixture was left stirring for another 2 h. The viscous gel-like syrup was then dried overnight at 130 ^oC and finally calcined at 400 ^oC for 1 h and 500 ^oC for 4 h to yield a voluminous powder.

For Pechini-glycerol (PCGL) and modified Pechini-glycerol (MPCGL), similar procedures to PC and MPC respectively were followed, the only difference being that glycerol was used instead of ethylene glycol as the polyol.

The prepared Pr-doped CeO_2 supports ($Ce_{0.9}Pr_{0.1}O_{2-\delta}$) were named as CSG, PC, MPC, PCGL and MPCGL, according to the method used for their synthesis. Ni was subsequently introduced via wet impregnation. $Ni(NO_3)_2{\cdot}6H_2O$ (Fluka, 97%) in a calculated amount (so as to obtain 10 wt% Ni in the final catalyst), was added in 100 ml d-H_2O. Afterwards, the metal oxide support was added. Water was removed in a rotary evaporator at 72 ^oC, followed by further drying at 90 ^oC overnight. Finally, calcination was carried out at 400 ^oC for 4 h. The resulting "calcined" catalysts were named as NiO/ Support. The "reduced" ones (Ni/ Support) were obtained following reduction at 500 ^oC for 1 h under H_2.

2.2. Characterization techniques

The instruments and methodology used for the characterization of the catalytic materials employed in this work can be found in Refs. [16, 17]. The following characterizations were employed: (i) XRD was used to examine the crystallinity of the catalysts. (ii) N_2 physisorption was used to determine the porous characteristics. (iii) H_2-TPR over the as-prepared (calcined) catalysts was employed for the investigation of the reducibility of the materials. (iv) The surface basicity of the reduced catalysts was determined using CO_2-TPD. (v) H_2-TPD was carried out to

determine the strength of H_2 interaction and calculate the dispersion of Ni and the Ni mean particle size. (vi) O_2-TPD was conducted to examine the oxygen storage capacity (OSC). (vii) Raman spectroscopy over the reduced catalysts was employed to study the oxygen environment. (viii) XPS analysis over the reduced catalysts was used to study the surface chemistry. Lastly, (ix) TEM was used to study the morphology of the supports and reduced catalysts. Regarding O_2-TPD, which was not performed in Refs. [16,17], an Autochem 2920 apparatus (Micromeritics, Atlanta, USA) was used. The samples were first pretreated at 300 °C for 1 h under He flow and then a 20% O_2/He flow was passed over the sample at 30 °C for 1 h, followed by a 15 min He purge. The temperature was then increased under He flow up to 800 °C (30 °C min^{-1} temperature ramp), while the thermal conductivity detector (TCD) signal was recorded continuously.

2.3. Catalytic testing

Catalytic testing was performed in a continuous flow fixed-bed quartz reactor (I.D. = 0.9 cm) at atmospheric pressure. The fresh (calcined) catalysts were initially reduced in situ under H_2 for 1 h at 500 °C. Catalytic activity/ stability was evaluated via three experimental protocols.

Under Experimental Protocol #1, catalytic activity evaluation was carried out by varying the reaction temperature at a weight hourly space velocity (WHSV) equal to 25,000 ml g_{cat}^{-1} h^{-1}, using 0.24 g of catalyst. The H_2:CO_2 ratio was 1:4 and the reaction temperature was increased from 200 to 450 °C using 50 °C intervals, while remaining for 30 min at each temperature to achieve steady-state. A higher WHSV of 100,000 ml g_{cat}^{-1} h^{-1} was used in Experimental Protocol #2. The only difference with Experimental Protocol #1, was that the catalyst loaded was now 0.06 g. This protocol was also used to calculate the CO_2 activation energy for CO_2 conversions below 20%, while assuming pseudo-first-order kinetics. The catalytic stability was evaluated under Experimental Protocol #3, with the temperature remaining at 350 °C for 24 h (WHSV = 25,000 ml g_{cat}^{-1} h^{-1}).

The outlet gas composition was analyzed online by gas chromatography, as described in Ref. [16]. The carbon balance was found to close at ± 3%. The following Eqs. (2)–(5) were used to calculate the CO_2 conversion, CH_4/CO selectivity and CH_4 yield:

$$X_{CO_2}(\%) = \frac{C_{CH_4}^{out} + C_{CO}^{out}}{C_{CO_2}^{out} + C_{CH_4}^{out} + C_{CO}^{out}} \cdot 100 \quad (2)$$

$$S_{CH_4}(\%) = \frac{C_{CH_4}^{out}}{C_{CH_4}^{out} + C_{CO}^{out}} \cdot 100 \quad (3)$$

$$S_{CO}(\%) = \frac{C_{CO}^{out}}{C_{CH_4}^{out} + C_{CO}^{out}} \cdot 100 \quad (4)$$

$$Y_{CH_4}(\%) = \frac{X_{CO_2} \cdot S_{CH_4}}{100} \quad (5)$$

with C^{out} being the concentration at the outlet of the reactor for each gas.

Finally, the consumption rate of CO_2, was calculated via Eq. (6):

$$r_{CO_2} = \left(\frac{X_{CO_2}}{100}\right) \cdot \left(\frac{F_{CO_2}}{W_{cat}}\right) \quad (6)$$

where X_{CO_2} is the CO_2 conversion (%), F_{CO_2} is the CO_2 molar flow rate at the inlet of the reactor (mol s^{-1}) and W_{cat} is the catalyst mass (g).

2.4. Modelling methodology

2.4.1. Reaction rates

CO_2 methanation is influenced by side-reactions, such as the reverse water-gas-shift (RWGS) reaction and CO methanation. In the most widely accepted mechanism of the CO_2 methanation reaction, the RWGS reaction competes with CO_2 methanation, reducing CO_2 to CO, which thereafter undergoes hydrogenation to CH_4 [41]. Thus, these three reactions, i.e., CO and CO_2 methanation and RWGS, were included in the design of the CFD model.

Xu and Froment [42] were some of the first who suggested the three-step model for the steam reforming of methane and their model has also been examined for CO_2 methanation by a number of scientists [41,43]. The kinetic model consists of the aforementioned three reactions occurring in parallel; the rate equations are given below (Eqs. (7)–(9)):

$$r_{CO2Meth.} = \frac{\frac{k_{CO_2Meth.}}{p_{H_2}^{3.5}}\left(p_{H_2}^4 p_{CO_2} - \frac{p_{CH_2}p_{H_2O}^2}{K_{eq,CO_2Meth.}}\right)}{\left(1 + K_{CO}p_{CO} + K_{H_2}p_{H_2} + K_{CH_4}p_{CH_4} + \frac{K_{H_2O}p_{H_2O}}{p_{H_2}}\right)^2} \quad (7)$$

$$r_{RWGS} = \frac{\frac{k_{RWGS}}{p_{H_2}}\left(p_{H_2}p_{CO_2} - \frac{p_{CO}p_{H_2O}}{K_{eq,RWGS}}\right)}{\left(1 + K_{CO}p_{CO} + K_{H_2}p_{H_2} + K_{CH_4}p_{CH_4} + \frac{K_{H_2O}p_{H_2O}}{p_{H_2}}\right)^2} \quad (8)$$

$$r_{COMeth.} = \frac{\frac{k_{COMeth.}}{p_{H_2}^{2.5}}\left(p_{H_2}^3 p_{CO_2} - \frac{p_{CO}p_{H_2O}}{K_{eq,COMeth.}}\right)}{\left(1 + K_{CO}p_{CO} + K_{H_2}p_{H_2} + K_{CH_4}p_{CH_4} + \frac{K_{H_2O}p_{H_2O}}{p_{H_2}}\right)^2} \quad (9)$$

where $k_{CO_2Meth.}$, k_{RWGS}, $k_{CO\ Meth.}$ represent the rate constants of reactions, expressed by the Arrhenius equation. K_{CO}, K_{H_2}, K_{CH_4} and K_{H_2O} stand for the adsorption equilibrium constant and p_{CO_2}, p_{CO}, p_{H_2}, p_{CH_4} and p_{H_2O} for the partial pressure of species.

Table 1 shows the kinetic constants used for the study and Table 2 shows the adsorption constants and pre-exponential factors upon which the CFD modelling is based.

2.4.2. CFD methodology

CFD models can be used to demonstrate the particle-fluid transport phenomena in a microreactor, offering an alternative solution that requires less effort and expense in comparison to experimental work and delivers comprehensive information on the spatiotemporal variation in species flows, concentrations and temperatures withing the reactor. The reaction kinetics are set up with the Chemistry interface and the mass transport of the reacting species in the reactor is modeled with the Transport of Diluted Species interface with the Reactive Pellet Bed feature, which accounts for diffusion, convection and reaction in diluted solutions.

For the work presented herein, a 2D CFD model was designed with the assumption that the concentration and temperature gradients within the reactor occur only in the axial direction. The transport mechanism operating in this direction is the overall flow, which is of plug flow type. Assumptions upon which the model was founded include: (a) application of steady-state and isothermal conditions, (b) the pressure drop along the length of the reactor is very small and it can be considered

Table 1
Rate constants used as input parameters for the described model.

T (°C)	$k_{CO_2Meth.}$ (mol s^3 kg^{-2} m^{-1})	k_{RWGS} (mol s kg^{-1} m^{-2})	$k_{CO\ Meth.}$ (mol s^3 kg^{-2} m^{-1})
200	4.61 ×10^{-5}± 2.31 ×10^{-6}	0.1374± 0.02	1.3118 ×10^{-4} ± 6.56 ×10^{-6}
250	3.36 ×10^{-5}± 1.242 ×10^{-5}	0.1965± 0.02967	1.3042 ×10^{-4}± 6.5 ×10^{-6}
300	3.838 ×10^{-5}± 1.24 ×10^{-5}	0.1963± 0.02963	1.2979 ×10^{-4}± 6.49 ×10^{-6}
350	3.835 ×10^{-5}± 1.238 ×10^{-5}	0.1961± 0.0296	1.2927 ×10^{-4}± 6.46 ×10^{-6}
400	3.396 ×10^{-5}± 7.58 ×10^{-6}	0.196± 0.02958	1.2882 ×10^{-4}± 6.441 ×10^{-6}
450	2.78 ×10^{-5}± 6.18 ×10^{-6}	0.1958± 0.02956	1.2844 ×10^{-4}± 6.42 ×10^{-6}

Table 2
Reaction adsorption constants and pre-exponential factors.

Intrinsic constants	Value
Adsorption constants	
K_{CO} (bar^{-1})	40.91± 3.2[42]
K_{H_2} (bar^{-1})	0.0296 ± 0.00237[42]
K_{CH_4} (bar^{-1})	0.1791 ± 0.014[42]
K_{H_2O}	0.4152 ± 0.0332[42]
Pre-exponential factors	
$k_{0CO_2Meth.}$ $(mol\ s^3\ kg^{-2}\ m^{-1})$	$3.473 \times 10^{-5} \pm 1.59 \times 10^{-5}$
k_{0RWGS} $(mol\ s\ kg^{-1}\ m^{-2})$	0.19 ± 0.033
$k_{0CO\ Meth.}$ $(mol\ s^3\ kg^{-2}\ m^{-1})$	$1.234 \times 10^{-5} \pm 1 \times 10^{-5}$

negligible, (c) ideal gas law is applicable for the gases, (d) there is a constant axial fluid velocity in the reactor with uniform physical properties and transport coefficients, and (e) the reaction zone in the reactor is packed with catalytic material in powdered form. The microreactor has a height of 90 mm and a length of 30 cm. The mass balance equation for the species in the catalyst bed is expressed as:

$$u_x \frac{\delta c_i}{\delta x} = D_{i,A} \frac{\delta^2 c_i}{\delta x^2} - J_i S_b \tag{10}$$

where, $D_{i,A}$ are the axial dispersion coefficients, respectively, J_i is the molar flux of i into the catalyst powder and S_b is the active specific surface area of the powder exposed to the reacting fluids in the packed bed, which are given by:

$$S_b = S(1-\varepsilon) \tag{11}$$

where, ε is the fractional voidage of packed bed and S is the specific surface area per unit volume of the catalyst powder in m^{-1}.

For spherical catalyst powder, this is given by:

$$S = \frac{3}{r_{pe}} \tag{12}$$

where, r_{pe} is the radius of powdered form catalyst.

At the pellet-fluid interface, a film condition assumption is made. The flux of mass across the pellet-fluid interface into the pellet is possibly rate determined by the resistance to mass transfer to the bulk fluid side. This resistance can be expressed in terms of external mass transfer coefficient:

$$J_i = h_i\left(c_i - c_{i,ps}\right) \tag{13}$$

$$h_i = \frac{Sh \cdot D_i}{2r_{pe}} \tag{14}$$

$$Sc = \frac{\mu}{\rho \cdot D_i} \tag{15}$$

$$Re = \frac{2r_p \cdot \rho \cdot u_x}{\mu} \tag{16}$$

$$Sh = 2 + 0.552 Re^{1/2} Sc^{1/3} \tag{17}$$

where, $c_{i,ps}$ is the concentration of the fluid at the catalyst powder surface, h_i is the external mass transfer coefficient, μ and ρ are the viscosity and density of the reacting fluids respectively. Schmidt (Sc), Reynolds (Re), and Sherwood (Sh) numbers are dimensionless parameters related to the mass transfer occurring at the pellet-fluid interface.

The reactor is packed with catalyst powder in which the chemical reaction that occurs is incorporated into the mass balances with the Reactive Pellet Bed feature in COMSOL. This feature has a predefined (1D) extra dimension on the normalized radius ($r = r_{dim}/r_{pe}$) of the catalyst. The mass balance inside the catalyst particle across a spherical shell is given by:

$$4\pi N\left\{ r^2 r_{pe}^2 \varepsilon_{pe} \frac{\partial c_{pe,i}}{\partial t} + \nabla \cdot \left(- r^2 D_{i,eff} \nabla c_{pe,i} \right) = r^2 r_{pe}^2 R_{pe} \right\} \tag{18}$$

where, N is the number of particles per unit volume of the packed bed, r is the radius of catalyst particle (dimensionless), $D_{i,eff}$ is the effective diffusion coefficient of chemical species i in the catalyst pores, $c_{pe,i}$ is the concentration of chemical species i in the catalyst particle in mol m^{-3}. R_{pe} is the reaction rate term (rate of the reaction per unit volume of the catalyst particle).

The effective diffusivities of the species i into the pores of the catalyst particles are calculated by relating the diffusion coefficient to either the bulk or the Knudsen diffusivity.

$$D_{i,eff} = \frac{D_{i,AB} \Phi_p \sigma_c}{\tau} \tag{19}$$

where, $D_{i,AB}$ is the bulk diffusivity of chemical species i, Φ_p is the particle porosity, σ_c is the constriction factor and τ the tortuosity.

The boundary conditions were used as per the following:

$$\text{at } x = 0;\ c_{H_2} = c_{H_{2,in}} \text{ and } c_{CO_2} = c_{CO_{2,in}} \tag{20}$$

$$\text{at } x = 30;\ \frac{\delta c_i}{\delta x} = 0 \tag{21}$$

$$at\ r = 1;\ c_{i,p} = c_{i,ps} \tag{22}$$

$$\text{at } r = 0;\ \frac{\delta c_{i,p}}{\delta r} = 0 \tag{23}$$

COMSOL Multiphysics software version 5.5 was employed to solve the problem using the mass balance equations combined with the appropriate boundary conditions. The geometry comprised a mesh consisting of 2700 domain elements and 180600 degrees of freedom and the solution was checked from 180600 to 361200 degrees of freedom. As no difference in the results was obtained, the CFD results were mesh independent. The variables, which were used to solve the models, are shown in Table 3.

2.4.3. Process simulation methodology

The fluid packages selected to solve the complex problems were Peng Robinson with RK-Aspen (Redlich-Kwong), as they can accurately predict the vapour-liquid equilibrium data of hydrocarbons at high temperatures and pressures. The RK-Aspen property method is based on the Redlich-Kwong-Soave equation of state [44].

$$P = \frac{RT}{V_m - b} - \frac{a}{V_m(V_m + b)} \tag{24}$$

Table 3
The parameters used for the CFD models.

Symbol	Value	Units	Description
$c_{CO_2,in}$	4.4643	mol/m^3	CO_2 inlet concentration
$c_{H_2,in}$	17.857	mol/m^3	H_2 inlet concentration
Q	100	ml/min	Total inlet flow rate
D_{CO_2}	0.728	cm^2/s	Diffusion coefficient of CO_2
D_{H_2}	3.233	cm^2/s	Diffusion coefficient of H_2
D_{CO}	0.875	cm^2/s	Diffusion coefficient of CO
D_{CH_4}	1.135	cm^2/s	Diffusion coefficient of CH_4
D_{H_2O}	0.899	cm^2/s	Diffusion coefficient of H_2O
$D_{CO_2,eff}$	0.0777	cm^2/s	Effective diffusion coefficient of CO_2
$D_{H_2,eff}$	0.3448	cm^2/s	Effective diffusion coefficient of H_2
$D_{CO,eff}$	0.0933	cm^2/s	Effective diffusion coefficient of CO
$D_{CH_4,eff}$	0.121	cm^2/s	Effective diffusion coefficient of CH_4
$D_{H_2O,eff}$	0.0959	cm^2/s	Effective diffusion coefficient of H_2O
ρ_b	12.575	kg/m^3	Density of the catalyst bed
ρ_{pe}	2273–4545	kg/m^3	Density of the catalyst pellet
ε_{pe}	0.25–0.27	–	Porosity of the pellet
ε_b	$1 - \rho_b/\rho_{pe}$	–	Void fraction of the catalyst bed

The main differences between the original Redlich–Kwong–Soave equation and the RK-ASPEN property method are in the location of the interaction parameters in the mixing rules, the type of temperature-dependency of the interaction parameters and the introduction of an additional parameter in the alpha function to account for polar compounds [45].

The Peng-Robinson equation of state is highly suited for handling systems, which contain hydrocarbons, water and air. The equation implemented was in the form shown below [46]:

$$P = \frac{RT}{v-b} - \frac{a(T)}{v(v+b)+b(v-b)} \tag{25}$$

$$b = 0.07780\frac{RT_c}{P_c} \tag{26}$$

$$a(T) = a(T_c)\cdot\alpha\left(T_{R,\omega}\right) \tag{27}$$

$$a(T_c) = 0.45724\frac{R^2{T_c}^2}{P_c} \tag{28}$$

$$Z_c = 0.307 \tag{29}$$

$$\alpha^{\frac{1}{2}}\left(T_{R,\omega}\right) = 1 + k\left(1 - T_R^{\frac{1}{2}}\right) \tag{30}$$

$$k = 037464 + 1.54226\omega - 0.26992\omega^2 \tag{31}$$

The reactor energy balance, coupled with the material balance, can determine the heating or cooling requirements. The energy balance for the packed bed reactor can be given as:

$$\frac{dT}{dW} = \frac{r'_A\Delta H_{Rx}(T) - \frac{Ua}{\rho_b}(T - T_a)}{\sum F_i C_{Pi}} \tag{32}$$

where T is the reaction temperature, r'_A is the rate of reaction, ΔH_{RX} is the constant heat of reaction, U is the overall heat transfer coefficient, T_a is the ambient temperature, C_{pi} is the average heat capacity of species i, a is the heat exchange area for the packed bed reactor, ρ_b is the is the bulk density of the catalyst and F_i is the molar flow rate [47].

3. Results and discussion

3.1. Characterization of the supports and Ni catalysts

XRD characterization of the reduced catalysts (Fig. 1a) reveals the presence of the crystalline phases of CeO_2 ($2\theta \approx 29^o$, 33^o, 47^o and 56^o) and metallic Ni ($2\theta \approx 44.5^o$ and 52^o). As shown in previous works [16, 17,48], Pr^{x+} cations can easily dissolve into the crystalline lattice of CeO_2, creating a $Ce_{1-x}Pr_xO_{2-\delta}$ solid solution. The most common oxidation state of Pr in the solid solution has been found to be 3+, with the larger Pr^{3+} cations (1.27 Å) being able to substitute the smaller Ce^{4+} cations (0.97 Å), causing an expansion of the CeO_2 lattice and a shift of the diffraction angles to lower values than those normally observed for pure CeO_2 [16,17,48]. As will be shown later, in our case, Pr is indeed homogeneously dispersed over the support and rather exists in the Pr^{3+} oxidation state, proving that Pr^{3+} can successfully dissolve into the ceria lattice and cause a lattice expansion. The diffractogram of $Ce_{0.9}Pr_{0.1}O_{2-\delta}$ prepared via citrate sol-gel, along with the corresponding Ni catalyst, are compared with that of a similarly prepared CeO_2 ($CeO_{2-\delta}$) reference,

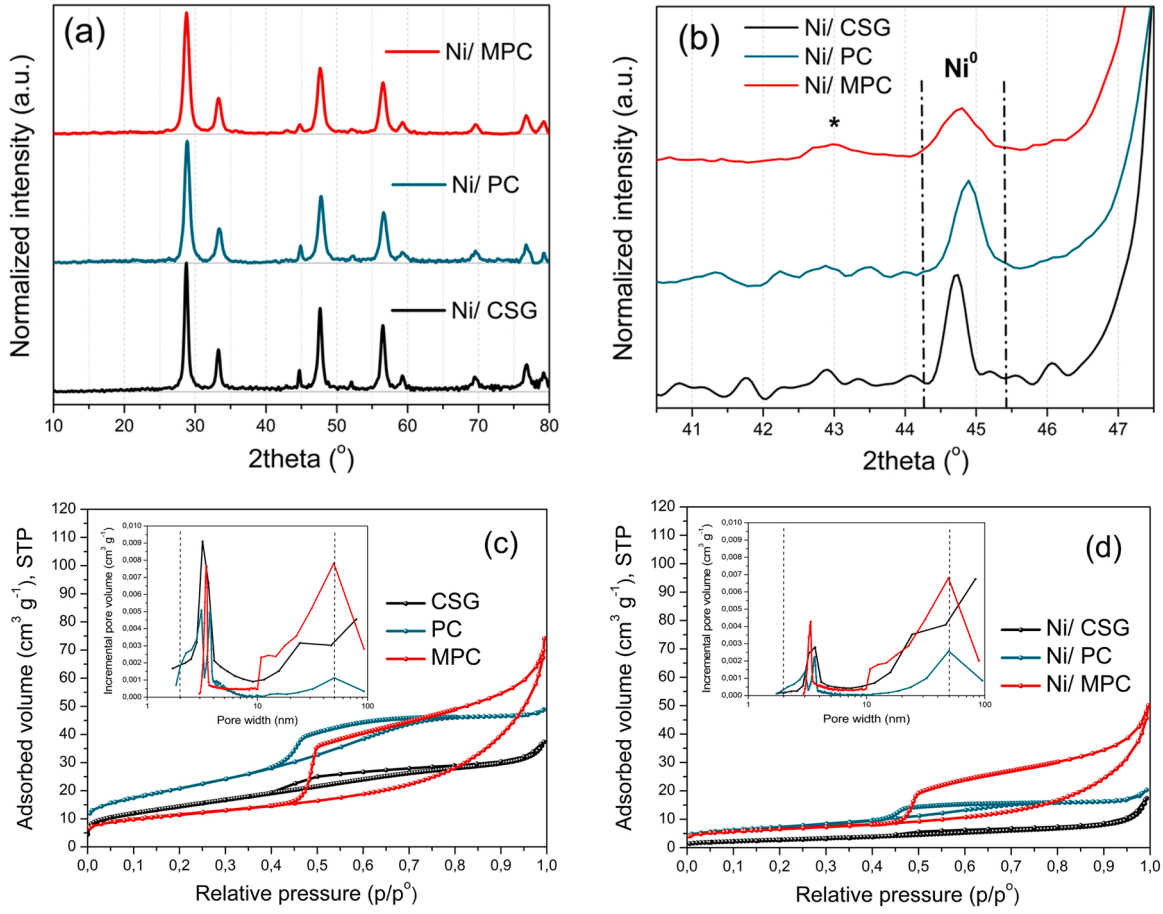

Fig. 1. (a-b) X ray diffractograms of the reduced catalysts with (b) focusing on the Ni^0 (111) reflection region. (c-d) N_2 physisorption isotherms and pore size distribution (inset) of (c) the supports and (d) the reduced catalysts.

with the (111) CeO_2 reflection shift toward smaller diffraction angles being apparent (Fig. S1). Moreover, some impregnated Ni^{2+} species could also dissolve into the lattice of the support, further affecting the support structure [49].

The crystallite size of the doped ceria support is reported in Table 4. It is quite similar for all the three different supports and catalysts, but we can observe a considerable drop when we compare the ceria crystallite size in the supports (7 nm) and the Ni impregnated and reduced catalysts (10–12 nm). A similar increase of the ceria crystallite size following Ni impregnation has also been reported elsewhere [17,49] and could be attributed to Ni^{2+} promoting the sintering of ceria, as well as to a possible ceria recrystallization during the impregnation step (dissolved $[Ni(H_2O)_6]^{2+}$ causing an acidic pH of the impregnation solution) [49,50]. Moreover, the H_2 reduction treatment can also cause a further growth of the ceria nanocrystallites [51]. In any case, the Ni impregnated catalysts have a quite similar ceria crystallite size (12 nm, 10 nm and 10 nm for Ni/CSG, Ni/PC and Ni/MPC respectively) but, as will be shown later, a quite different catalytic activity, meaning that the ceria support crystallite size exerts a rather minor influence on the catalytic performance.

Regarding the Ni^0 (111) reflection (Fig. 1b), one can observe a clear broadening in the case of the Ni/MPC catalyst, compared to the other two catalysts, indicating a much smaller Ni crystallite size in this case. The Ni^0 crystallite size was calculated by applying the Scherrer equation on the most intense (111) reflection. It was found to be 12 nm for Ni/MPC, 18 nm for Ni/PC and 19 nm for Ni/CSG (Table 4). Therefore, it is clear that the modified Pechini (MPC) synthesis method for the support can act to suppress the growth of the Ni crystallites and thus gives rise to a lower crystallite size of the impregnated Ni nanoparticles, improving their dispersion; the latter can be conducive toward a better catalytic performance [9,10,23]. Furthermore, the XRD pattern of Ni/MPC reveals the additional presence of the NiO phase ($2\theta \approx 43^o$), which could as well be present in the other two catalysts, possibly resulting from the partial oxidation of Ni following air exposure. In any case, the presence of Ni^{2+} species is not necessarily detrimental to the catalytic performance, as Cárdenas-Arenas et al. [24] have shown that high CO_2 methanation activity can best be achieved via a compromise in the population of Ni-O-Ce and Ni^0 sites.

N_2 physisorption was carried out to examine the textural properties of both the prepared supports, as well as the reduced catalysts, following the introduction of Ni. Regarding the prepared supports (Fig. 1c), one can observe the effect of the applied synthesis method on the porosity and pore structure of the synthesized mixed oxide. Citrate sol-gel (CSG) leads to a structure with a modest porosity (44 $m^2\ g^{-1}$), consisting of some micropores and small mesopores (3–4 nm), along with some larger mesopores and small macropores. Pechini (PC) method leads to a higher surface area (75 $m^2\ g^{-1}$), with a lesser contribution of larger pores (10–100 nm) compared to micropores and small mesopores. Both CSG and PC supports exhibit an H3-type hysteresis loop with slit pores [52]. Although the surface area of the support prepared via the modified Pechini (MPC) method is not particularly high (40 $m^2\ g^{-1}$), MPC leads to a much larger pore volume (Table 4), with the contribution of large mesopores (≈10–50 nm) and small macropores (50–100 nm) being much more pronounced. The contribution of small mesopores is also significant, as an H2(b)-type hysteresis loop is observed due to pore blocking upon desorption, which suggests the presence of a non-uniform porous network with interconnected pores of different sizes (connected ink-bottle pores) [52]. Pore size distribution (PSD) plots constructed upon employing different theories are also presented in Fig. S2.

Following $Ni(NO_3)_2{\cdot}6H_2O$ impregnation, calcination and reduction, the porous characteristics are altered (Fig. 1d). The greatest changes are observed for the Ni/CSG and Ni/PC catalysts, as Ni introduction causes a significant collapse of the porous structure, leading to a surface area drop by 82% and 65% respectively and a pore volume drop by 50% and 63% respectively. The micropores and small mesopores are more easily blocked upon Ni incorporation [53,54], as evidenced by the significant shift of the pore size distribution toward larger pore diameters. For the Ni/MPC catalyst, the introduction of Ni causes a much more modest drop in the surface area and pore volume (43% and 36% respectively), as the original support structure contained a higher number of large mesopores and small macropores (10–100 nm), which are not easily blocked by the medium-sized Ni nanoparticles [54]. Overall, the introduction of metallic Ni nanoparticles in the MPC support did not cause a major alteration of the porous structure, while it induces a significant structural collapse in the CSG and PC supports, due to blockage of the smaller pores.

The reducibility of the supports and fresh (calcined) catalysts was investigated via H_2 temperature programmed reduction (H_2-TPR, Fig. 2a). The peaks observed in the H_2-TPR profiles of the prepared supports (CSG, PC and MPC) are due to the removal of surface oxygen (O_S) at lower temperatures (< 550 °C) and bulk oxygen (O_B) at higher temperatures (> 550 °C) [23,24]. The total hydrogen consumption follows the trend (PC > CSG > MPC), which is correlated to the surface area of the supports (Table 4). This is expected, as a higher surface area can increase the number of surface defects and reactive surface oxygen species, and additionally shorten the diffusion pathways for the removal of bulk oxygen [23,24,26,27]. The higher surface area and smaller pore sizes in CSG and PC also appear to cause the removal of surface and bulk oxygen at lower temperatures compared to MPC [24].

When the reducibility of the calcined catalysts was examined, three reduction regimes could be observed; the first one due to reduction of highly dispersed NiO, $Ni(OH)_2$ and Ni^{2+} species, the second one accounting for the majority reduction of NiO nanoparticles into metallic Ni ones and the third one due to the removal of bulk oxygen from the doped ceria support [16–18,23,24]. The removal of surface oxygen from the support is expected to overlap with the main NiO reduction event at approx. 300–320 °C (region II). It can be observed, that the peak area (and thus H_2 consumption) for NiO/MPC is higher than that of the other two catalysts, which could be ascribed to the higher participation of the reduction of the support via the Ni-catalyzed ceria reduction [24]. A higher Ni dispersion in NiO/MPC can increase the number of Ni-O-Ce interfacial sites and thus, the contribution of Ni-catalyzed ceria reduction to the H_2 consumption. Following peak area integration, the amount of H_2 consumed for the three catalysts in regions I and II was calculated at 2.16, 2.21 and 2.38 mmol g^{-1} for NiO/CSG, NiO/PC and NiO/MPC respectively. When compared to the H_2 amount required to reduce all Ni^{2+} species to metallic Ni^0 (1.70 mmol g^{-1}), the aforementioned values correspond to 127%, 130% and 140% Ni^{2+} reduction for NiO/CSG, NiO/PC and NiO/MPC respectively. The excess H_2 amount is consumed via the Ni-catalyzed ceria reduction and is indeed higher for NiO/MPC, which presents the greatest Ni dispersion.

The surface basicity of the reduced catalysts is indicative of their

Table 4
Crystallite sizes of CeO_2 and Ni^0 (Φ_{CeO2} and Φ_{Ni}) determined via the Scherrer equation from XRD. Specific surface area (SSA), pore volume (V_P) and average pore diameter (D_{ave}) calculated via N_2 physisorption. Ni dispersion (D_{Ni}) and particle size (d_{Ni}) determined via H_2-TPD. O_2 desorption determined via O_2-TPD. Values are for the reduced catalysts and in parentheses for the supports.

Sample name	Φ_{CeO2} (nm)	Φ_{Ni} (nm)	SSA ($m^2\ g^{-1}$)	V_P ($cm^3\ g^{-1}$)	D_{ave} (nm)	D_{Ni} (%)	d_{Ni} (nm)	O_2 desorbed (mmol g^{-1})
Ni/CSG	12 (7)	19	8 (44)	0.03 (0.06)	13 (5)	4.0	24	0.13 (0.14)
Ni/PC	10 (7)	18	26 (75)	0.03 (0.08)	5 (4)	4.9	20	0.16 (0.17)
Ni/MPC	10 (7)	12	23 (40)	0.07 (0.11)	13 (11)	6.1	16	0.20 (0.22)

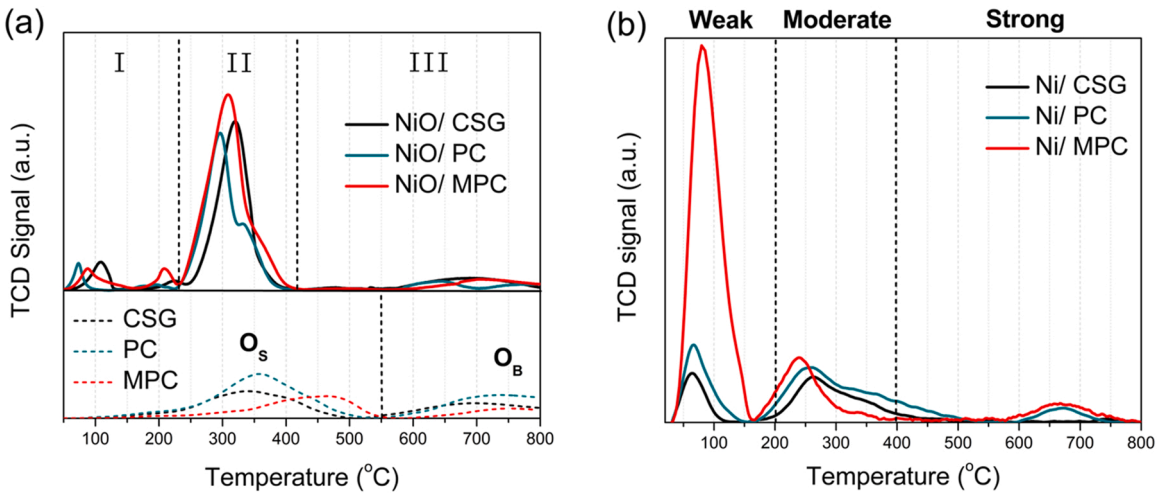

Fig. 2. (a) H_2-TPR profiles of the supports and calcined catalysts. (b) CO_2-TPD profiles of the reduced catalysts.

potential for CO_2 chemisorption and activation [11]. CO_2 can be adsorbed on a plethora of different sites on Ni/CeO_2-type catalysts, including metallic Ni sites, Ni-O-Ce interfacial sites, as well as on the surface oxygen vacancies of the Pr-doped CeO_2 support [11,15,17,24]. It can either be adsorbed as bicarbonates/ mono- or bidentate carbonates, or as CO via dissociative adsorption [55]. Upon the desorption of CO_2 observed during the CO_2-TPD profiles (Fig. 2b), the emerged peaks can be assigned to weak basic sites (< 200 °C), moderately strong basic sites (200–400 °C) and strong basic sites (> 400 °C), depending on the temperature of the observed CO_2 desorption [16–18,56,57].

It is evident, that although the amount of strong basic sites and moderately strong basic sites is similar for all catalysts, Ni/MPC contains roughly six times higher amount of weak basic sites (based on peak area integration), compared to the other two catalysts. The weak basic sites can generally be assigned to surface hydroxyl groups (-OH) and other oxygen species formed from weakly adsorbed oxygen on surface oxygen vacancies and Ni-O-Ce interfacial sites, to which CO_2 can be adsorbed in the form of bicarbonates [16,23,56]. As such, they can be correlated to the textural characteristics of the respective catalyst and the Ni dispersion. Ni/MPC better retains its textural properties (surface area, pore volume) following Ni impregnation and also exhibits a higher Ni dispersion and, as a result, a higher population of Ni-O-Ce interfacial sites, which also act to increase the overall weak basicity of this catalyst. According to Ma et al. [56], a larger population of weak basic sites is conducive toward a higher CO_2 methanation activity, as they can act to accelerate the initial step of CO_2 chemisorption, bringing it in close proximity to the methanation active sites during the reaction [24,56].

Calculation of the Ni dispersion and the mean Ni particle size was realized via H_2-TPD experiments (Fig. S3a). Desorption peaks were observed both at the low-temperature regime (< 200/250 °C), due to the desorption of hydrogen species weakly bonded to the metallic Ni nanoparticles, and at the high-temperature regime (> 200/250 °C), due to the desorption of hydrogen species with a stronger Ni-H binding [17,58,59]. Generally, the majority of desorbed hydrogen was observed at low temperatures, whereas for the Ni/MPC catalyst a slight shift of the desorption peaks toward lower temperatures was observed, indicating a weaker Ni-H interaction [58]. The calculated values for Ni dispersion and mean Ni particle size, based on peak area integration, can be found in Table 4. Ni/MPC was shown to exhibit a higher Ni dispersion and reduced Ni particle size, in line with the results obtained via XRD characterization. Finally, the fact that the mean Ni particle sizes calculated via H_2-TPD were larger compared to the mean Ni crystallite sizes calculated via the Scherrer equation (XRD) can be explained by a partial covering of the Ni nanoparticles by $CeO_{2-\delta}$ entities, which can limit the available hydrogen chemisorption sites, as reported by other works [60].

O_2-TPD was used to examine the oxygen storage capacity (OSC) of the supports and catalysts (Fig. S3b). The oxygen species desorbed at various temperatures can generally be divided into two categories, i.e., surface oxygen (O_S, also denoted as α-oxygen), which is desorbed at lower temperatures, and bulk oxygen (O_B, also denoted as β-oxygen), which is desorbed at temperatures higher than 500/550 °C [22,26,61,62]. Since multiple peaks can be observed below 550 °C, surface oxygen can be further subdivided into weakly adsorbed oxygen species on oxygen vacancies (incl. physically adsorbed oxygen, surface hydroxyl groups (-OH) and O^{2-}/ O^- species, O_{S1}) and surface lattice oxygen (O_{S2}) [61,62]. The amount of O_2 desorbed (in mmol g^{-1}, Table 4) during the O_2-TPD profiles can be associated with the oxygen storage capacity (OSC) of the materials, and this value is higher for the Ni/MPC catalyst (and the MPC support) compared to the other materials. Moreover, the Ni/MPC catalyst displays a much higher amount of weakly adsorbed oxygen species (O_{S1}), which can be associated with oxygen vacancies and surface defects [22,26,27,61,63].

Raman spectroscopy (Fig. S4) reveals a similar defect structure in all of the three supports and catalysts with the same Pr loading (10 mol%), as shown by the peak centred around 550 cm^{-1} in the so-called defects' region [16]. This peak can be deconvoluted into two bands, at around 535 cm^{-1} and 590 cm^{-1} respectively (Fig. S4c). The larger deconvoluted band at around 535 cm^{-1} is the extrinsic vacancy band, since the introduction of Pr'_{Ce} substitutional defects is charge compensated by the creation of extrinsic oxygen vacancies (O_V) [16,18]. The second, smaller band at around 590 cm^{-1} is ascribed to the presence of a PrO_x hetero-phase (likely Pr_6O_{11}) with Pr atoms in octahedral coordination with oxygen atoms (PrO_8), due to the small degree of Pr-segregation at the support grains [17]. Since the O_V band is much larger than the PrO_8 band, we can deduce that the majority of Pr atoms are solubilized in the CeO_2 structure, participating in the oxygen vacancy formation [17]. Moreover, the dominant F_{2G} peak, which for pure CeO_2 is normally observed at approx. 450–460 cm^{-1}, is significantly red-shifted at approx. 420–430 cm^{-1} for Pr-doped CeO_2 and Ni supported on Pr-doped CeO_2, due to the incorporation of larger Pr^{3+} (and to a lesser extent Ni^{2+}) cations in the CeO_2 structure [16–18].

It should be first noted, that XPS analysis for the reduced catalysts was carried out following exposure to atmospheric conditions (ex-situ). The core level XPS spectra for Ni 2p and Ce 3d are presented in Fig. 3, while those for O 1 s and Pr 3d are given in Fig. S4. Table S1 contains the values for the surface elemental composition. As observed in other works [16–18,24], the surface concentration of Ni is mostly higher than its nominal value, since Ni preferentially resides on the catalyst surface as metallic and/or oxidized nickel nanoparticles. The surface concentration of Ni is the highest for Ni/PC (followed by Ni/CSG) and the

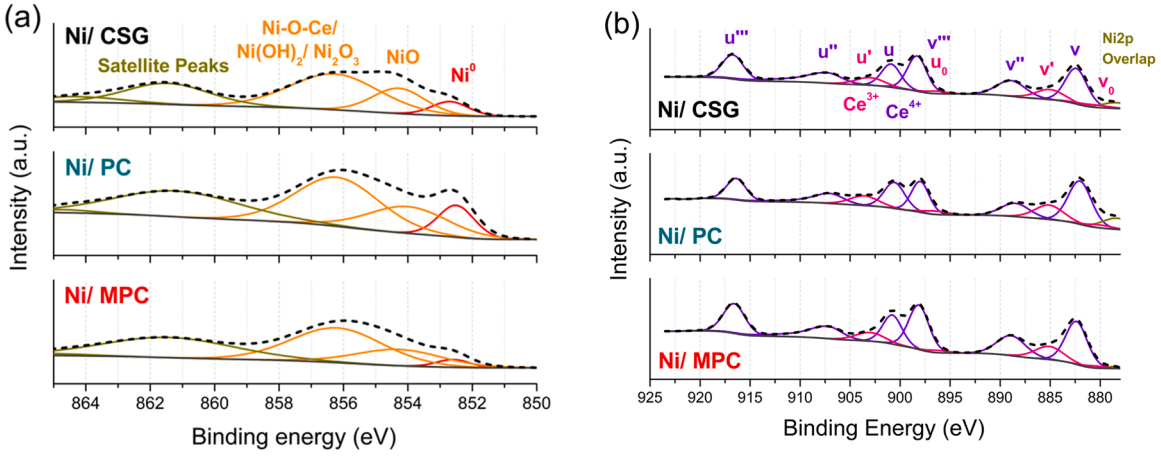

Fig. 3. XPS core level spectra of the reduced catalysts. (a) Ni 2p and (b) Ce 3d.

lowest for Ni/MPC, which could be a result of a higher Ni dispersion along the porosity of the support in the latter case [17,24]. The concentration of Pr at the surface in relation to Ce is also higher than anticipated by the $Ce_{0.9}Pr_{0.1}O_{2-\delta}$ support nominal stoichiometry, since Pr'_{Ce} defects have been shown to preferentially reside at the surface of the solid solution [64].

The deconvoluted Ni 2p XPS spectra are depicted in Fig. 3a. They show that metallic Ni is more prominent on the Ni/PC and Ni/CSG reduced catalysts, while Ni/MPC exhibits less metallic Ni and a much higher contribution of oxidized Ni^{x+}. Oxidized Ni^{x+} species can be further separated into two contributions; the lower BE (binding energy) peak due to supported bulk NiO and the higher BE peak due to Ni-O-Ce interfacial sites, $Ni(OH)_2$, Ni^{2+} dissolved in the metal oxide and Ni^{3+} species, which can arise from defects in the NiO phase [16,17,65–67]. The fact that metallic Ni, in relation to oxidized Ni, has a much lower contribution in Ni/MPC compared to the other two catalysts (Table S1) can be attributed to the fact that the smaller and more well-dispersed Ni^0 nanoparticles over Ni/MPC can be more easily oxidized upon air exposure, which proceeded the ex-situ XPS characterization [17,24]. This can also be the reason for the observation of a NiO reflection ($2\theta \approx 43^o$) in the X-ray diffractogram of the Ni/MPC catalyst (Fig. 1b).

Fig. 3b shows the Ce 3d XPS spectra, that can be deconvoluted into 10 different peaks (5 doublets), with v, v'', v''', u, u'' and u''' assigned to Ce^{4+}, which constitute the majority of Ce species found in CeO_2-based oxides and v_0, v', u_0 and u' assigned to Ce^{3+}, which arise as intrinsic Ce'_{Ce} defects due to the high reducibility and oxygen lability of CeO_2 [16,17,22]. The Ce^{3+} contribution is slightly more pronounced in Ni/PC (Table S1). For the purpose of this work however, where a Pr-doped $Ce_{0.9}Pr_{0.1}O_{2-\delta}$ support is used, the oxygen lability of the metal oxide support is mainly associated with the extrinsic Pr'_{Ce} defects, which are charge compensated by the emergence of oxygen vacancies and thereby, oxygen deficiency (δ) [16,17,48,64]. Extrinsic Pr'_{Ce} defects can generate oxygen vacancies ($V_{\ddot{O}}$), while maintaining the neighbouring Ce cations in the 4+ state [48,64].

The O 1 s XPS peaks arising from the various oxygen species can be found in Fig. S5a. The low BE peak (≈ 529 eV) is observed due to the support lattice oxygen [17,49,66]. The neighbouring peak at higher BE (≈ 531.5 eV) can be attributed to weakly adsorbed oxygen species and surface hydroxides/ carbonates arising from the air exposure of the catalyst prior to the XPS measurement [17,49,66]. Finally, physisorbed water can be observed at higher BE, at around 533 eV [17,49]. Regarding the Pr 3d peaks (Fig. S5b), they closely resemble the XPS spectrum of Pr_2O_3, meaning that the oxidation state of Pr in the catalysts is rather Pr^{3+} [64,68]. Therefore, in agreement with the Raman results (Fig. S4), the majority of Pr cations are expected to be incorporated into the CeO_2 lattice as extrinsic Pr'_{Ce} defects, with only a minority being segregated on the support grains as PrO_x (Pr_6O_{11}) in a rather octahedral coordination with oxygen atoms [17,64]. When comparing the different catalysts, the position of the Pr 3d peaks is slightly shifted for Ni/CSG and Ni/PC toward higher BE, compared to the peak position of Ni/MPC. This is indicative of a slightly higher oxidation state of Pr in Ni/CSG and Ni/PC and thus, of a higher amount of surface segregated PrO_x (Pr_6O_{11}) oxides, which could hinder the Ni-CeO_2 interaction [17,64,68,69]. On the other hand, a higher percentage of Pr cations in Ni/MPC appear incorporated in the support structure as Pr^{3+}, thereby participating in the oxygen vacancy formation and maintaining the Ni-CeO_2 contact [17,69].

TEM images of the sol-gel prepared Pr-doped CeO_2 oxides (Fig. 4a-c) reveal that the supports consist of spongy aggregates of small crystallites. CSG and PC (prepared via citrate sol-gel and Pechini methods respectively) have a much spongier network structure, which contains a very high number of small pores (up to 5 nm in diameter). MPC however, which was prepared via the H_2O-free modified Pechini method, exhibits a greatly altered pore structure. The porous structure in this case consists of larger pores and large pore openings (≈30 nm) can be visible in Fig. 4c. Therefore, the synthesis procedure, and more specifically the properties of the citrate/ polymeric gel, appear to affect the material structure during sol-gel synthesis [25,27]. The more compact citrate/ polymeric xerogels following water evaporation during CSG and PC synthesis lead to spongier aggregates with smaller pores, whereas the combustion of the viscous polymeric gel following the MPC synthesis yields a more well-defined porous structure with larger pores and a higher degree of order. This can be attributed to the different chemical environment following complexation of the metal cations and formation of the polymer precursor during the support synthesis, which can in turn influence the nucleation and growth of the metal oxide crystallites during the calcination process, as well as lead to the formation of larger voids/ pores upon the combustion of more bulky organic groups [27,70,71]. Additional TEM images of the prepared supports can be sought after in Fig. S6.

The dispersion of the Ni nanoparticles in the reduced catalysts can be found in Fig. 4d-l. From the bright field TEM images (Fig. 4d-f), the supported Ni nanoparticles are made visible and, at first glance, appear smaller for the Ni/MPC catalyst and larger for the Ni/PC one. HAADF-STEM coupled with EDS mapping (Fig. 4g-l) was subsequently conducted. In the case of Ni/CSG and Ni/PC, it reveals the presence of large Ni aggregates with a non-uniform size distribution (size polydispersity), along with some smaller Ni nanoparticles. In contrast, medium-sized and well-dispersed Ni nanoparticles with a more uniform size distribution, which are confined inside the porous network, are visible for the Ni/MPC catalyst. An explanation is that Ni impregnation causes severe pore blockage in the Ni/CSG and Ni/PC catalysts, with Ni forming large

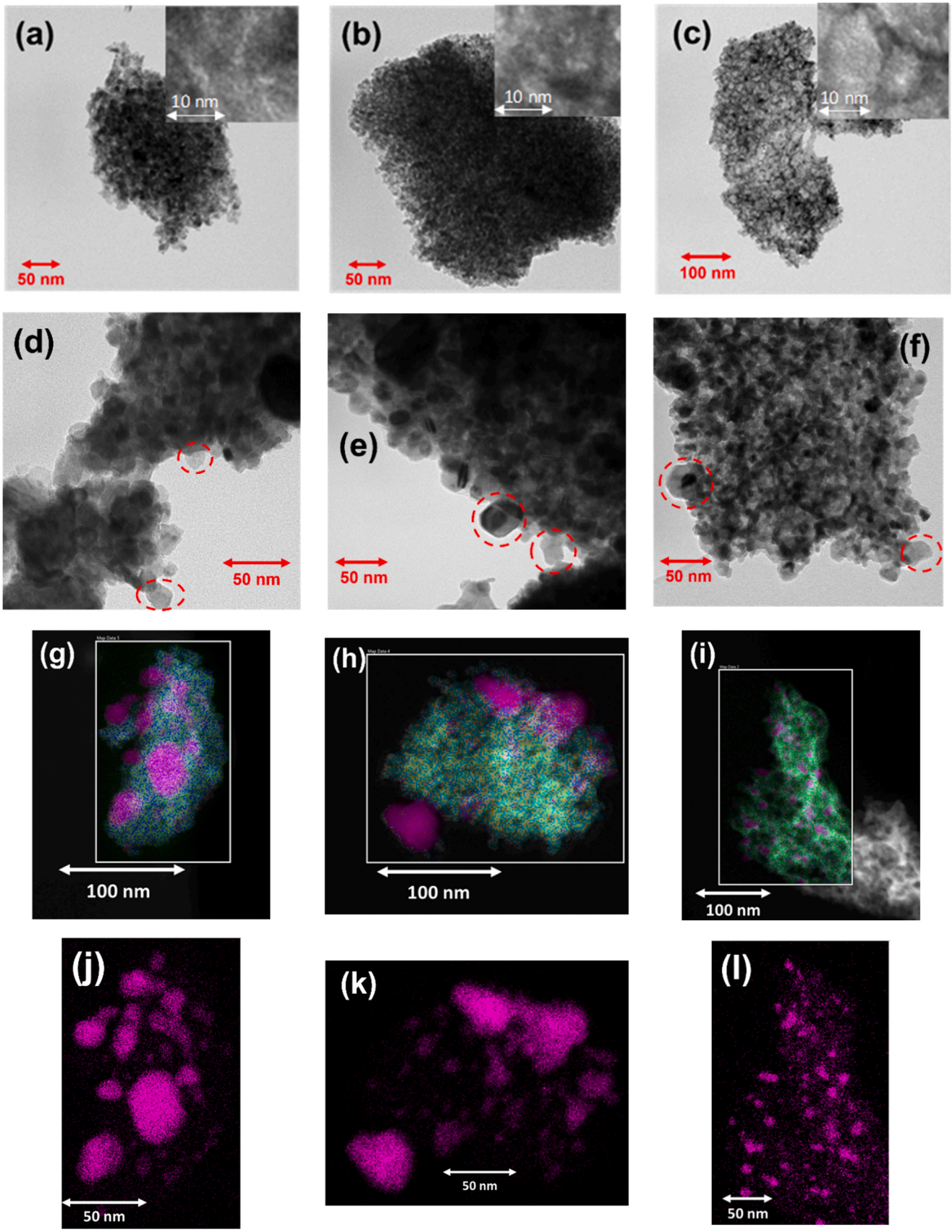

Fig. 4. Electron microscopy characterization: (a-c) TEM images of the CSG, PC and MPC supports respectively. (d-f) TEM images, (g-i) HAADF-STEM images along with EDS elemental mapping and (j-l) EDS elemental mapping regarding the Ni element for the Ni/CSG, Ni/PC and Ni/MPC reduced catalysts respectively.

and sintered aggregates following high temperature calcination and reduction processes (400 °C and 500 °C respectively) [53,54]. This is further corroborated by the N_2 physisorption results (Fig. 1c-d), where a sharp drop in the surface area and pore volume is observed for these catalysts. On the other hand, the improved wetting upon impregnation and the larger and better-ordered pores in the MPC support led to a much more reduced pore blockage in the Ni/MPC catalyst and a more uniform dispersion of the medium-sized Ni nanoparticles inside the pore walls of the porous structure [54]. HAADF-STEM coupled with EDS mapping for all the elements (Ce, Pr, Ni and O) for the Ni/MPC catalyst can be found in Fig. S7. Moreover, Ni nanoparticle size distribution histograms and tentative mean Ni nanoparticle size estimates for the three catalysts considering the Ni EDS mapping images are provided in Fig. S8.

3.2. Evaluation of the catalytic performance

The catalysts were first evaluated under Experimental Protocol #1, where the CO_2 methanation performance was studied while varying the reaction temperature (Fig. 5). A comparison between the CO_2 conversion and CH_4 selectivity/ yield values for the three catalysts can be found in Table 5. The variation of CH_4 yield with temperature can be found in Fig. S9. In general, Ni/CSG prepared via the citrate sol-gel method was fairly active and selective toward CH_4. The use of the typical Pechini method to prepare the CeO_2-based support does not appear to promote the catalytic activity, as Ni/PC presents a worse performance to Ni/CSG in terms of CO_2 conversion and CH_4 selectivity. This can be attributed to the larger pore volume loss upon Ni impregnation and a less favourable Ni-CeO_2 interaction [24,54]. In contrast, the modified Pechini synthesis method (MPC) offers a great improvement in the CO_2 methanation catalytic performance of the Ni/MPC catalyst, by substantially enhancing the low-temperature CO_2 conversion and promoting CH_4 selectivity. In any case, the thermodynamic equilibrium curve is not reached, even for the most active Ni/MPC catalyst. This is however a quite usual phenomenon in the relevant literature regarding the CO_2 methanation reaction, as the maximum attainable CO_2 conversion value also depends on the experimental conditions used (e.g., the weight hourly space velocity) [16–18,22,23,56,72].

It is already established in the literature, that medium-sized (10–25 nm) Ni nanoparticles dispersed over CeO_2 are the optimal to achieve a high CO_2 methanation activity [22,57,72]. A smaller Ni nanoparticle size promotes the selectivity toward CO, while larger Ni nanoparticles greatly reduce the available active surface sites [72]. Moreover, a delicate balance between Ni-O-Ce interfacial sites and Ni^0 metallic sites needs to be achieved, as the former are considered active for the CO_2 activation and the latter for H_2 activation [15,24]. Thus, the improved catalytic performance of the Ni/MPC catalyst can be attributed to its physicochemical characteristics, as the MPC support exhibits a well-ordered structure with large pores, highly suitable for the deposition of medium-sized and well-dispersed Ni nanoparticles (Fig. 4) [23,54]. The medium-sized Ni nanoparticles nanoconfined into the porous structure offer a multitude of active metallic and interfacial sites for the CO_2 methanation reaction, as well as easy access and diffusion for the reactant and product gases [15,23,24]. A comparison between the catalytic performance of our best-performing Ni/MPC catalyst and that of other catalysts reported in the literature is provided in tabular form in the supplementary material (Table S2). It can be observed, that Ni/MPC does indeed compare favourably with other CO_2 methanation catalysts that have a similar composition and were tested under similar conditions, in terms of CO_2 conversion and CH_4 selectivity.

Table 5
CO_2 methanation performance at 350 °C and in parenthesis, at 300 °C (Experimental Protocol #1).

Catalyst name	CO_2 conversion (%)	CH_4 selectivity (%)	CH_4 yield (%)
Ni/ CSG	70 (46)	98 (98)	69 (45)
Ni/ PC	61 (33)	97 (97)	59 (32)
Ni/ MPC	77 (71)	99 (99)	76 (70)

Until now, we have shown that the pore structure and pore volume modification of the support, induced via the addition of ethylene glycol and the use of a modified Pechini synthesis route can greatly impact the catalytic performance of the supported Ni catalysts. Since Kayaalp et al. [26] and Poffe et al. [27] have demonstrated the ability to further tune the textural properties by substituting ethylene glycol with other polyols, the Ni/PCGL and Ni/MPCGL catalysts were prepared similarly to Ni/PC and Ni/MPC, but with the use of glycerol instead of ethylene glycol during the support synthesis (as described in the Experimental Part). The catalytic activity results can be sought after in Fig. S10. Although Ni/PCGL was superior to Ni/PC, especially in terms of low-temperature CO_2 conversion, Ni/MPCGL prepared via the modified Pechini method using glycerol failed to provide an improvement to the Ni/MPC catalyst. As both of these catalysts prepared with glycerol (Ni/PCGL and Ni/MPCGL) were inferior to the already studied Ni/MPC and Ni/CSG, they were not evaluated/ characterized further.

Experimental Protocol #2 was then employed to study the CO_2 methanation performance under less favourable conditions (higher WHSV of 100,000 ml g_{cat}^{-1} h^{-1}) and construct Arrhenius plots for the CO_2 activation energy calculation, while assuming pseudo-first-order kinetics and for CO_2 conversion values < 20% (Fig. 6). Although, as expected, the overall catalytic activity and CH_4 selectivity is worse when the space velocity is increased [17,22], the differences in catalytic performance between the three catalysts become more apparent. CH_4 selectivity is especially affected in the case of Ni/PC, as a reduced

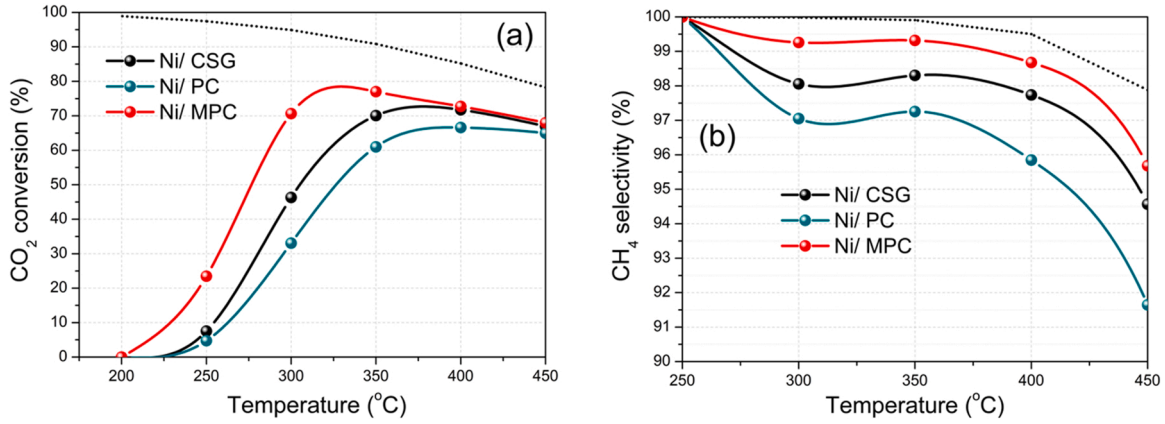

Fig. 5. Catalytic performance of the reduced catalysts while varying the reaction temperature (Experimental Protocol #1): (a) CO_2 conversion and (b) CH_4 selectivity. Thermodynamic equilibrium values calculated using Aspen Plus (H_2:CO_2 = 4:1 and p = 1 atm) are represented by the dotted lines.

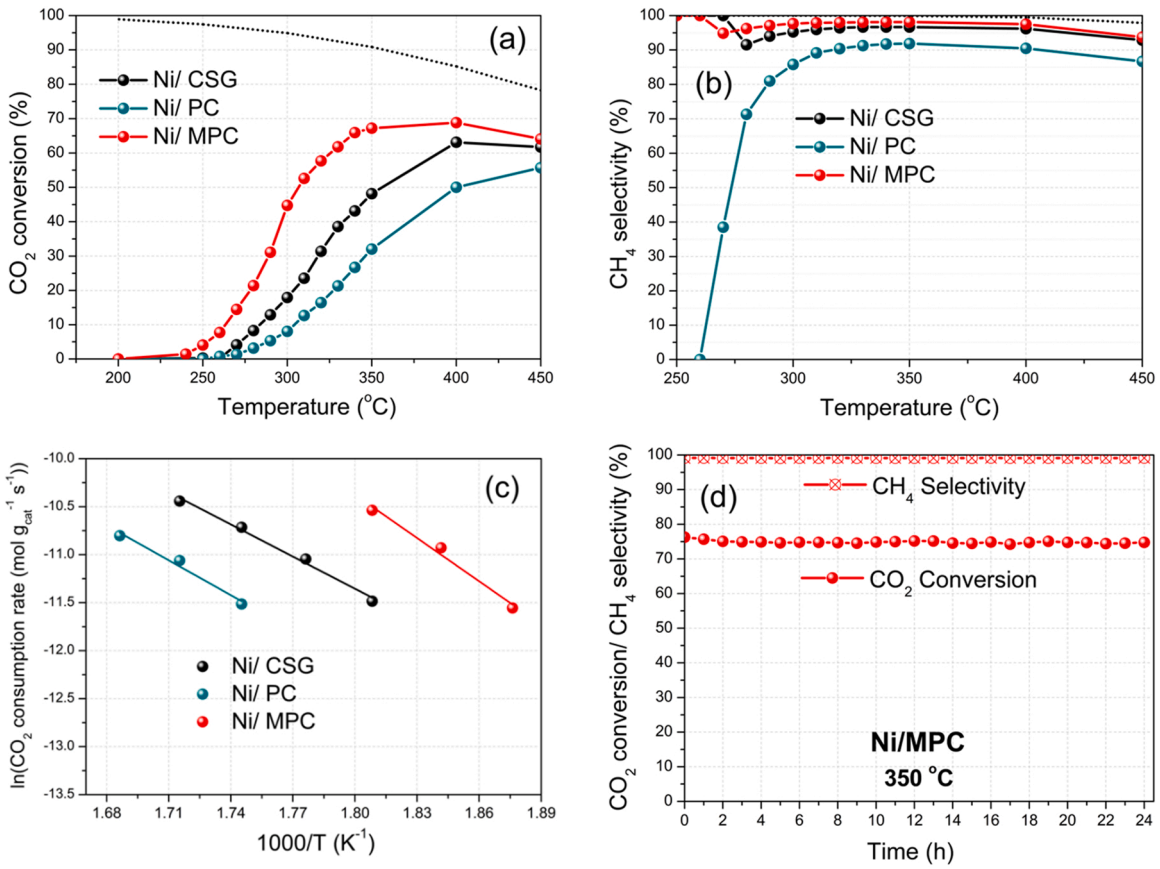

Fig. 6. (a) CO_2 conversion and (b) CH_4 selectivity as a function of reaction temperature (Experimental Protocol #2). (c) Natural logarithm of the forward CO_2 consumption rates as a function of reciprocal temperature. (d) Time-on-stream catalytic performance (CO_2 conversion and CH_4 selectivity) for the Ni/MPC catalyst at 350 °C (Experimental Protocol #3). Thermodynamic equilibrium values calculated using Aspen Plus (H_2:CO_2 = 4:1 and p = 1 atm) are represented by the dotted lines.

contact time favours the desorption of CO intermediates at lower temperatures [73].

Interestingly, as can be observed by the slopes of the regression lines in the Arrhenius plots (Fig. 6c), the CO_2 activation energy of the most active Ni/MPC catalyst is calculated higher than that of the other two catalysts (CO_2 activation energy was calculated for Ni/MPC at 125 kJ mol^{-1}, compared to 101 kJ mol^{-1} for Ni/PC and 93 kJ mol^{-1} for Ni/CSG). These CO_2 activation energy (E_a) values are in line with the available literature regarding Ni/CeO_2-type catalysts (E_a values of approx. 90–130 kJ mol^{-1}) [21,57,72,74–76]. In general however, the CO_2 activation energy provides a metric of how sensitive a CO_2 methanation catalyst is with respect to changes in the reaction temperature and does not constitute a good descriptor of the CO_2 methanation catalytic activity [74,77]. As an example, CO_2 activation energies for Ni/Al_2O_3 are often reported to be lower than those for Ni/CeO_2, despite the fact that the Ni/CeO_2 system is demonstrated to be greatly

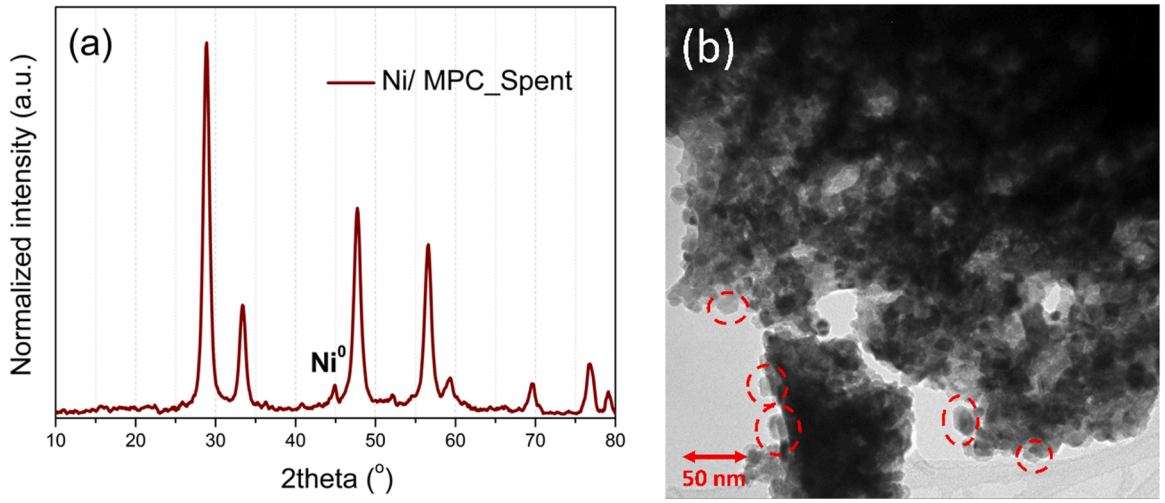

Fig. 7. (a) X-ray diffractogram and (b) TEM image of the spent Ni/ MPC catalyst (Results obtained for sample tested under Experimental Protocol #3).

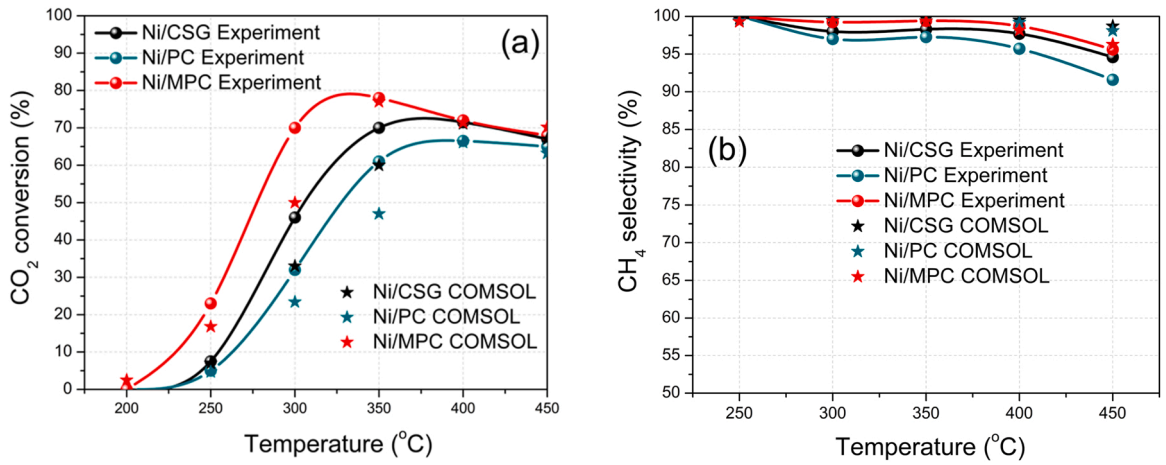

Fig. 8. Comparison between experimental results and CFD model results. (a) CO_2 conversion and (b) CH_4 selectivity as a function of reaction temperature (Experimental Protocol #1).

superior to Ni/Al_2O_3 with a similar Ni loading [15,74,77].

Lastly, the catalytic stability of the most active Ni/MPC catalyst was evaluated at 350 °C for 24 h under Experimental Protocol #3 (Fig. 6d). CO_2 conversion dropped by less than 2%, stabilizing at around 75%, while CH_4 selectivity stabilized at roughly 99%. This proves that Ni/MPC can provide a good and stable catalytic performance, which can last for an extended period of time.

3.3. Spent catalyst characterization

The physicochemical characteristics of the Ni/MPC catalyst after the 24 h time-on-stream test (Figs. 7 and S11) were studied in order to examine possible catalyst degradation phenomena. The XRD of the spent catalyst is quite similar to that of the reduced one, with the Ni crystallite size being calculated at ≈11 nm (Scherrer). N_2 physisorption confirmed a stable porous structure (SSA = 24 m^2/g, V_P = 0.08 cm^3/g and D_{ave} = 13 nm), while the Raman spectrum reveals the preservation of the oxygen vacancy population. Finally, TEM imaging does not reveal any significant change in morphology compared to the reduced catalyst, with Ni nanoparticles well-dispersed and confined inside the structured porous network. Therefore, the Ni/MPC spent catalyst characterization provides a further testament to the superior stability of this catalyst, as it can preserve its crystallinity, porosity, defect chemistry, Ni dispersion and structural integrity after several hours under the reactant stream, all the while providing a good and stable catalytic performance. All the aforementioned reasons render this catalyst (Ni/MPC) a viable candidate for further scaled-up testing under industrially relevant conditions, as well as for potential industrial implementation.

3.4. Computational modelling

The results obtained from the CFD models were compared to the experimental data. The designed microreactor was operated at a pressure of 1 atm and temperatures from 200 to 450 °C and tested for both Experimental Protocols #1 and #2. The comparison between the experimental and simulated results gives an indicator of the validity of the model.

We first turn our attention to the comparison between the experimental and simulated results carried out under the Experimental Protocol's #1 reaction conditions. Fig. 8 shows the conversion of CO_2 and the selectivity for CH_4 and, as can be observed, there is good agreement between the experimental results and the obtained CFD results. The average conversion deviation was found to be less than 12% for all three catalysts, while the average selectivity deviation was less than 3%. The results show, that as the temperature increases, the conversion of CO_2 also increases, reaching a maximum conversion around 325 °C (Fig. 8a). Above this temperature, a decrease of the conversion is observed (Fig. 8a), suggesting that the reverse activation energy is lowered, i.e., the reverse reaction (producing CO_2) becomes more favourable than the forward reaction (consuming CO_2) at higher temperatures. As for the selectivity toward CH_4, this decreases as the temperature increases, in good agreement with the reaction thermodynamics and the experimental results, while it remains at very high values for all three catalysts. As it can be seen, the computational validation for the three catalysts is very good, with the predictions for Ni/MPC being the closest to the experimentally obtained results, in comparison to the other two catalysts.

Fig. 9 shows the comparison between the experimental and simulated results for Experimental Protocol #2 and, in particular, the conversion of CO_2 (Fig. 9a), the selectivity for CH_4 (Fig. 9b) and the consumption rate of CO_2 (Fig. 9c). As expected, decreasing the catalyst weight (i.e., increasing the WHSV) leads to lower overall values in terms of the conversion of CO_2. It is also noted, that the decrease in the conversion of CO_2 at higher temperatures, observed during Experimental Protocol #1, appears shifted at slightly higher temperatures (i.e., around 375 °C). By the slopes of the regression lines in Fig. 9c, the CO_2 activation energy of each catalyst, based on the simulated results, can be found. These values for Ni/CSG, Ni/PC and Ni/MPC were found to be 55, 56 and 117 kJ mol^{-1} respectively, values that deviate from the experimental results, possibly due to the different side-reactions occurring within the reactor (although the trend between the different catalysts is the same).

The validity and robustness of the models were assessed by comparing the CFD results with the process simulation modelling results. Fig. 10a-b shows the effect of temperature on the conversion of CO_2 and selectivity for CH_4, using a WHSV of 25,000 ml g_{cat}^{-1} h^{-1}. Fig. 10c-d shows the effect of temperature on the conversion of CO_2 and selectivity for CH_4, using a WHSV of 100,000 ml g_{cat}^{-1} h^{-1}. It can be observed, that both models have a similar performance under constant modelling conditions. Therefore, both models have the ability to

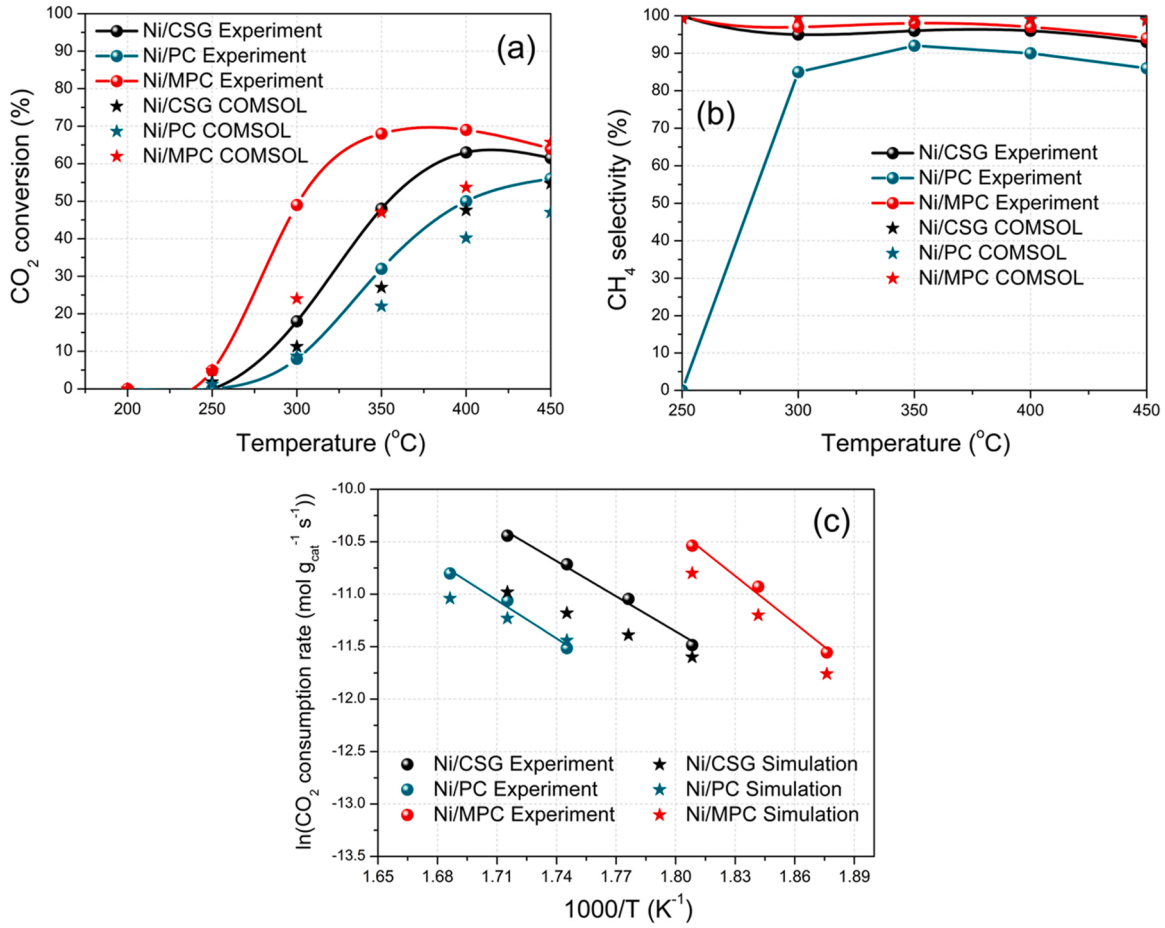

Fig. 9. Comparison between experimental results and CFD model results. (a) CO_2 conversion and (b) CH_4 selectivity as a function of reaction temperature. (c) Natural logarithm of the forward CO_2 consumption rates as a function of reciprocal temperature (Experimental Protocol #2).

successfully predict the methanation of CO_2 using Ni catalysts. Moreover, both computational modelling approaches can successfully predict the CO_2 conversion and CH_4 selectivity.

The dynamic process simulation model was able to assess the catalytic stability of the Ni/MPC catalyst, using constant modelling conditions at 350 °C (Experimental Protocol #3, Fig. 11). The results show an excellent validation between the modelling and experimental results. Consequently, the dynamic process simulation model can successfully predict the stable catalytic performance of the Ni/MPC catalyst. Further computational modelling analysis was performed to assess the internal and external mass transfer limitations, which is described in the supplementary material (Fig. S12 and S13).

4. Conclusions

This work reported on the modification of the porous characteristics and architecture of Pr-doped CeO_2 oxides via the alteration of the sol-gel type preparation method. Citrate sol-gel and conventional Pechini led to spongy crystalline aggregates with reduced pore size and volume. On the other hand, the H_2O-free modified Pechini method led to a nanostructure with increased pore openings and pore volume. The higher pore size and volume, along with the more ordered nanostructure, were beneficial toward the formation of medium-sized Ni nanoparticles following impregnation, which were confined into the pore structure. In contrast, larger metallic Ni aggregates were formed on the oxides with a reduced pore size. Most importantly, the greater Ni dispersion and enhanced porosity of the Ni/MPC catalyst (support prepared via modified Pechini) acted to increase the population of surface defects and weak basic sites, which improve the CO_2 chemisorption and activation over this catalyst.

The more favourable architecture and physicochemical properties of the Ni/MPC catalyst manifested themselves into a greatly improved CO_2 methanation catalytic performance (> 50% increase in CO_2 conversion at 300 °C compared to Ni/CSG, whose support was prepared via citrate sol-gel). Moreover, this catalyst was found to be highly stable at 350 °C, with CO_2 conversion and CH_4 selectivity remaining constant at around 75% and 99% respectively, whereas the catalyst nanostructure and properties remained unchanged following the stability experiment.

CFD modelling was also conducted to simulate the catalytic performance. The observed experimental and simulated results showed good agreement, with the Ni/MPC catalyst having the best performance when compared to the other two catalysts. The dynamic process simulation model could also successfully predict the stability of the Ni/MPC catalyst.

In short, the current work shows that the catalyst nanostructure and active metal dispersion play a crucial role toward the design of CO_2 methanation catalysts. As CO_2 methanation greatly depends upon the availability and ratio of CO_2 and H_2 chemisorption sites, a well-desired catalyst architecture would be a porous catalyst consisting of relatively medium-sized and well-dispersed metal nanoparticles, coupled with a high population of surface defects and basic sites. Modification of sol-gel type syntheses via the introduction of different chelating/ crosslinking agents is a simple and straightforward method to produce metal oxide supports with a quasi-tailored nanoporosity, which are conducive toward the deposition of medium-sized metallic nanoparticles of the desired size, as a result leading to highly active transition metal-based CO_2 methanation catalysts.

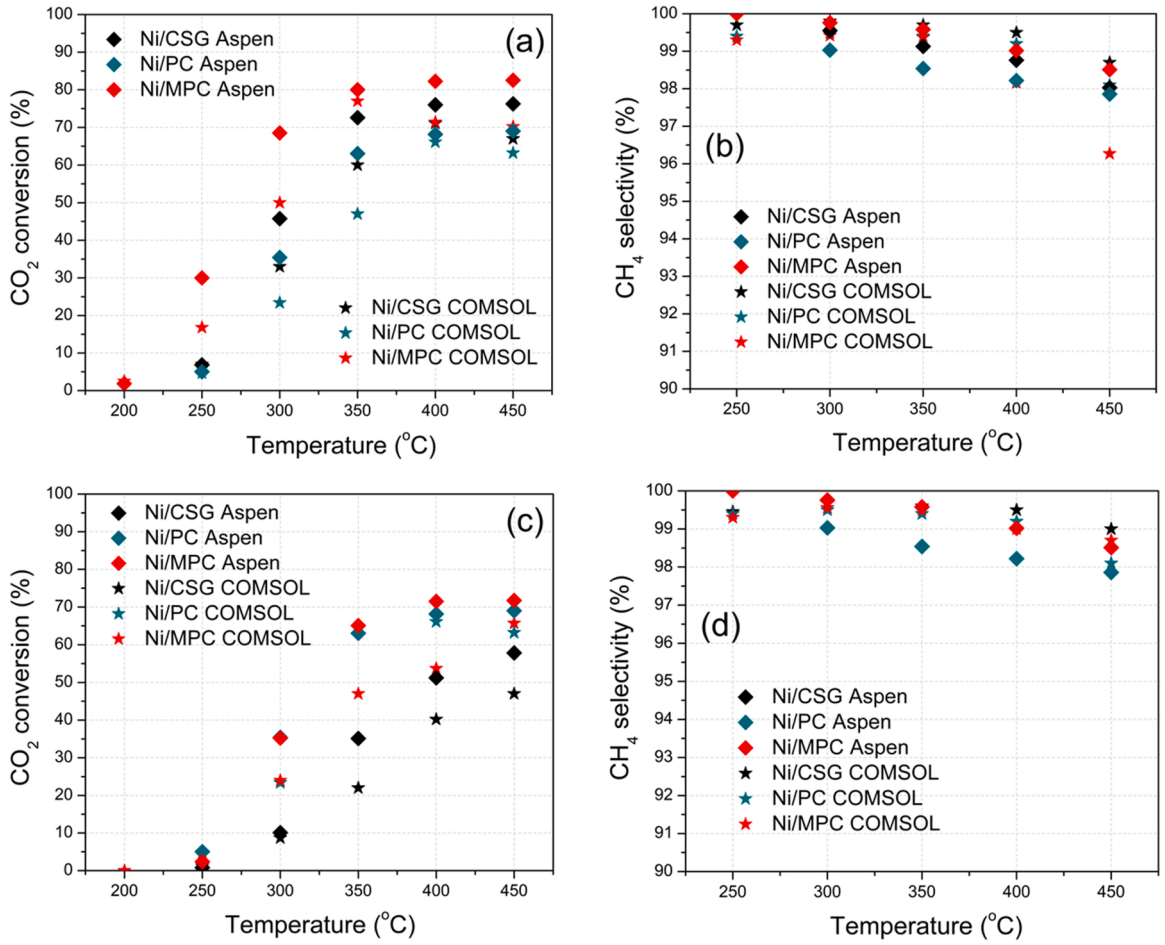

Fig. 10. Comparison between CFD and process simulation modelling results. (a) CO_2 conversion and (b) CH_4 selectivity as a function of reaction temperature (Experimental Protocol #1). (c) CO_2 conversion and (d) CH_4 selectivity as a function of reaction temperature (Experimental Protocol #2).

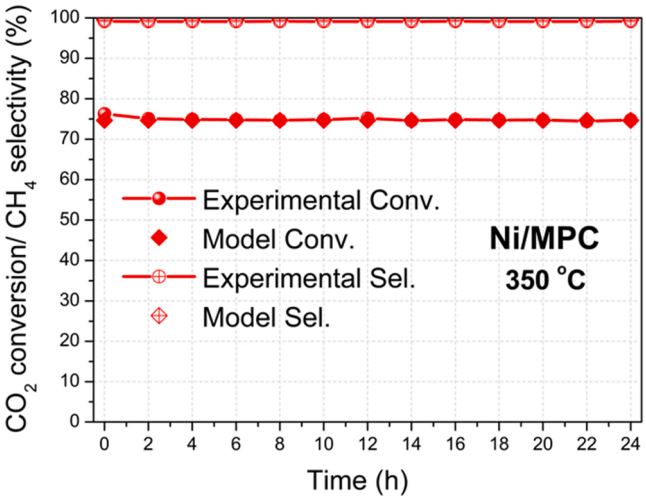

Fig. 11. Modelling validation of the time-on-stream catalytic performance (CO_2 conversion and CH_4 selectivity) for the Ni/MPC catalyst at 350 °C (Experimental Protocol #3).

CRediT authorship contribution statement

Anastasios I. Tsiotsias: Conceptualization, Methodology, Validation, Investigation, Writing – original draft. **Nikolaos D. Charisiou:** Investigation, Writing – review & editing, Supervision, Project administration. **Eleana Harkou:** Investigation, Writing – original draft. **Sanaa Hafeez:** Investigation, Writing – original draft. **George Manos:** Writing – review & editing. **Achilleas Constantinou:** Writing – review & editing. **Aseel G.S. Hussien:** Investigation. **Aasif A. Dabbawala:** Investigation. **Victor Sebastian:** Investigation. **Steven J. Hinder:**

Investigation. **Mark A. Baker:** Investigation, Writing – review & editing. **Kyriaki Polychronopoulou:** Investigation, Writing – review & editing, Funding acquisition. **Maria A. Goula:** Writing – review & editing, Supervision, Project administration, Funding acquisition.

Declaration of Competing Interest

The authors declare that they have no known competing financial interests or personal relationships that could have appeared to influence the work reported in this paper.

Data availability

Data will be made available on request.

Acknowledgements

AIT, NDC and MAG acknowledge support of this work by the project "Development of new innovative low carbon energy technologies to improve excellence in the Region of Western Macedonia" (MIS 5047197), which is implemented under the Action "Reinforcement of the Research and Innovation Infrastructure" funded by the Operational Program "Competitiveness, Entrepreneurship and Innovation" (NSRF 2014–2020) and co-financed by Greece and the European Union (European Regional Development Fund). AGSH, AAD and KP acknowledge support from Khalifa University through the grant RC2–2018-024. Additional partial support has been provided by the Abu Dhabi Award for Research Excellence (AARE) 2019 through project AARE19–233. VS acknowledges the ICTS ELECMI-LMA for offering access to their instruments and expertise.

Appendix A. Supporting information

Supplementary data associated with this article can be found in the online version at doi:10.1016/j.apcatb.2022.121836.

References

[1] C. Breyer, M. Fasihi, C. Bajamundi, F. Creutzig, Direct air capture of CO_2: a key technology for ambitious climate change mitigation, Joule 3 (2019) 2053–2057, https://doi.org/10.1016/j.joule.2019.08.010.

[2] F. Nocito, A. Dibenedetto, Atmospheric CO_2 mitigation technologies: carbon capture utilization and storage, Curr. Opin. Green. Sustain. Chem. 21 (2020) 34–43, https://doi.org/10.1016/j.cogsc.2019.10.002.

[3] A. Al-Mamoori, A. Krishnamurthy, A.A. Rownaghi, F. Rezaei, Carbon capture and utilization update, Energy Technol. 5 (2017) 834–849, https://doi.org/10.1002/ente.201600747.

[4] P. Gao, L. Zhang, S. Li, Z. Zhou, Y. Sun, Novel heterogeneous catalysts for CO_2 hydrogenation to liquid fuels, ACS Cent. Sci. 6 (2020) 1657–1670, https://doi.org/10.1021/acscentsci.0c00976.

[5] L. Zhang, Y. Dang, X. Zhou, P. Gao, A. Petrus van Bavel, H. Wang, S. Li, L. Shi, Y. Yang, E.I. Vovk, Y. Gao, Y. Sun, Direct conversion of CO_2 to a jet fuel over CoFe alloy catalysts, Innov 2 (2021), 100170, https://doi.org/10.1016/j.xinn.2021.100170.

[6] D. Hidalgo, J.M. Martín-Marroquín, Power-to-methane, coupling CO_2 capture with fuel production: An overview, Renew. Sustain. Energy Rev. 132 (2020), 110057, https://doi.org/10.1016/j.rser.2020.110057.

[7] S. Hafeez, E. Harkou, S.M. Al-Salem, M.A. Goula, N. Dimitratos, N.D. Charisiou, A. Villa, A. Bansode, G. Leeke, G. Manos, A. Constantinou, Hydrogenation of carbon dioxide (CO_2) to fuels in microreactors: a review of set-ups and value-added chemicals production, React. Chem. Eng. (2022) 795–812, https://doi.org/10.1039/d1re00479d.

[8] C. Vogt, M. Monai, G.J. Kramer, B.M. Weckhuysen, The renaissance of the Sabatier reaction and its applications on Earth and in space, Nat. Catal. 2 (2019) 188–197, https://doi.org/10.1038/s41929-019-0244-4.

[9] M.C. Bacariza, D. Spataru, L. Karam, J.M. Lopes, C. Henriques, Promising catalytic systems for CO_2 hydrogenation into CH_4: A review of recent studies, Processes 8 (2020) 1646, https://doi.org/10.3390/pr8121646.

[10] W.K. Fan, M. Tahir, Recent trends in developments of active metals and heterogenous materials for catalytic CO2hydrogenation to renewable methane: A review, J. Environ. Chem. Eng. 9 (2021), 105460, https://doi.org/10.1016/j.jece.2021.105460.

[11] A.I. Tsiotsias, N.D. Charisiou, I.V. Yentekakis, M.A. Goula, The role of alkali and alkaline earth metals in the CO_2 methanation reaction and the combined capture and methanation of CO_2, Catalysts 10 (2020) 812, https://doi.org/10.3390/catal10070812.

[12] A.I. Tsiotsias, N.D. Charisiou, I.V. Yentekakis, M.A. Goula, Bimetallic Ni-based catalysts for CO_2 methanation: A review, Nanomaterials 11 (2021) 28, https://doi.org/10.3390/nano11010028.

[13] L. Shen, J. Xu, M. Zhu, Y.F. Han, Essential role of the support for nickel-based CO_2 methanation catalysts, ACS Catal. 10 (2020) 14581–14591, https://doi.org/10.1021/acscatal.0c03471.

[14] S. Tada, T. Shimizu, H. Kameyama, T. Haneda, R. Kikuchi, Ni/CeO_2 catalysts with high CO_2 methanation activity and high CH_4 selectivity at low temperatures, Int. J. Hydrog. Energy 37 (2012) 5527–5531, https://doi.org/10.1016/j.ijhydene.2011.12.122.

[15] A. Cárdenas-Arenas, A. Quindimil, A. Davó-Quiñonero, E. Bailón-García, D. Lozano-Castelló, U. De-La-Torre, B. Pereda-Ayo, J.A. González-Marcos, J. R. González-Velasco, A. Bueno-López, Isotopic and in situ DRIFTS study of the CO_2 methanation mechanism using Ni/CeO_2 and Ni/Al_2O_3 catalysts, Appl. Catal. B Environ. 265 (2020), 118538, https://doi.org/10.1016/j.apcatb.2019.118538.

[16] G.I. Siakavelas, N.D. Charisiou, S. AlKhoori, A.A. AlKhoori, V. Sebastian, S. J. Hinder, M.A. Baker, I.V. Yentekakis, K. Polychronopoulou, M.A. Goula, Highly selective and stable nickel catalysts supported on ceria promoted with Sm_2O_3, Pr_2O_3 and MgO for the CO_2 methanation reaction, Appl. Catal. B Environ. 282 (2021), 119562, https://doi.org/10.1016/j.apcatb.2020.119562.

[17] A.I. Tsiotsias, N.D. Charisiou, A. AlKhoori, S. Gaber, V. Stolojan, V. Sebastian, B. van der Linden, A. Bansode, S.J. Hinder, M.A. Baker, K. Polychronopoulou, M. A. Goula, Optimizing the oxide support composition in Pr-doped CeO_2 towards highly active and selective Ni-based CO_2 methanation catalysts, 561–547, J. Energy Chem. 71 (2022), https://doi.org/10.1016/j.jechem.2022.04.003.

[18] G.I. Siakavelas, N.D. Charisiou, A. AlKhoori, S. AlKhoori, V. Sebastian, S.J. Hinder, M.A. Baker, I.V. Yentekakis, K. Polychronopoulou, M.A. Goula, Highly selective and stable Ni/La-M (M=Sm, Pr, and Mg)-CeO_2 catalysts for CO_2 methanation, J. CO_2 Util. 51 (2021), 101618, https://doi.org/10.1016/j.jcou.2021.101618.

[19] A. Vita, C. Italiano, L. Pino, P. Frontera, M. Ferraro, V. Antonucci, Activity and stability of powder and monolith-coated Ni/GDC catalysts for CO_2 methanation, Appl. Catal. B Environ. 226 (2018) 384–395, https://doi.org/10.1016/j.apcatb.2017.12.078.

[20] C. Sun, P. Beaunier, V. La Parola, L.F. Liotta, P. Da Costa, Ni/CeO_2 nanoparticles promoted by yttrium doping as catalysts for CO_2 methanation, ACS Appl. Nano Mater. 3 (2020) 12355–12368, https://doi.org/10.1021/acsanm.0c02841.

[21] N. Hashimoto, K. Mori, K. Asahara, S. Shibata, H. Jida, Y. Kuwahara, H. Yamashita, How the Morphology of NiO_x-Decorated CeO_2 Nanostructures Affects Catalytic Properties in CO_2 Methanation, Langmuir 37 (2021) 5376–5384, https://doi.org/10.1021/acs.langmuir.1c00546.

[22] Y. Du, C. Qin, Y. Xu, D. Xu, J. Bai, G. Ma, M. Ding, Ni nanoparticles dispersed on oxygen vacancies-rich CeO_2 nanoplates for enhanced low-temperature CO_2 methanation performance, Chem. Eng. J. 418 (2021), 129402, https://doi.org/10.1016/j.cej.2021.129402.

[23] P. Hongmanorom, J. Ashok, P. Chirawatkul, S. Kawi, Interfacial synergistic catalysis over Ni nanoparticles encapsulated in mesoporous ceria for CO_2 methanation, Appl. Catal. B Environ. 297 (2021), 120454, https://doi.org/10.1016/j.apcatb.2021.120454.

[24] A. Cárdenas-Arenas, A. Quindimil, A. Davó-Quiñonero, E. Bailón-García, D. Lozano-Castelló, U. De-La-Torre, B. Pereda-Ayo, J.A. González-Marcos, J. R. González-Velasco, A. Bueno-López, Design of active sites in Ni/CeO_2 catalysts for the methanation of CO_2: Tailoring the Ni-CeO_2 contact, Appl. Mater. Today 19 (2020), 100591, https://doi.org/10.1016/j.apmt.2020.100591.

[25] A.E. Danks, S.R. Hall, Z. Schnepp, The evolution of "sol-gel" chemistry as a technique for materials synthesis, Mater. Horiz. 3 (2016) 91–112, https://doi.org/10.1039/c5mh00260e.

[26] B. Kayaalp, S. Lee, K. Klauke, J. Seo, L. Nodari, A. Kornowski, W.C. Jung, S. Mascotto, Template-free mesoporous $La_{0.3}Sr_{0.7}Fe_xTi_{1-x}O_{3\pm\delta}$ with superior oxidation catalysis performance, Appl. Catal. B Environ. 245 (2019) 536–545, https://doi.org/10.1016/j.apcatb.2018.12.077.

[27] E. Poffe, H. Kaper, B. Ehrhardt, L. Gigli, D. Aubert, L. Nodari, S. Gross, S. Mascotto, Understanding oxygen release from nanoporous perovskite oxides and its effect on the catalytic oxidation of CH_4 and CO, ACS Appl. Mater. Interfaces 13 (2021) 25483–25492, https://doi.org/10.1021/acsami.1c02281.

[28] S. Hafeez, E. Aristodemou, G. Manos, S.M. Al-Salem, A. Constantinou, Computational fluid dynamics (CFD) and reaction modelling study of bio-oil catalytic hydrodeoxygenation in microreactors, React. Chem. Eng. 5 (2020) 1083–1092, https://doi.org/10.1039/d0re00102c.

[29] S. Hafeez, E. Aristodemou, G. Manos, S.M. Al-Salem, A. Constantinou, Modelling of packed bed and coated wall microreactors for methanol steam reforming for hydrogen production, RSC Adv. 10 (2020) 41680–41692, https://doi.org/10.1039/d0ra06834a.

[30] S. Hafeez, F. Sanchez, S.M. Al-Salem, A. Villa, G. Manos, N. Dimitratos, A. Constantinou, Decomposition of additive-free formic acid using a Pd/C catalyst in flow: Experimental and CFD modelling studies, Catalysts 11 (2021) 341, https://doi.org/10.3390/catal11030341.

[31] S. Hafeez, S.M. Al-Salem, K.N. Papageridis, N.D. Charisiou, M.A. Goula, G. Manos, A. Constantinou, Theoretical investigation of the deactivation of ni supported catalysts for the catalytic deoxygenation of palm oil for green diesel production, Catalysts 11 (2021) 747, https://doi.org/10.3390/catal11060747.

[32] S. Hafeez, S.M. Al-Salem, A. Bansode, A. Villa, N. Dimitratos, G. Manos, A. Constantinou, Computational Investigation of Microreactor Configurations for Hydrogen Production from Formic Acid Decomposition Using a Pd/C Catalyst, Ind. Eng. Chem. Res. 61 (2022) 1655–1665, https://doi.org/10.1021/acs.iecr.1c04128.

[33] E. Harkou, S. Hafeez, G. Manos, A. Constantinou, CFD study of the numbering up of membrane microreactors for CO_2 capture, Processes 9 (2021) 1515, https://doi.org/10.3390/pr9091515.

[34] N. Engelbrecht, S. Chiuta, R.C. Everson, H.W.J.P. Neomagus, D.G. Bessarabov, Experimentation and CFD modelling of a microchannel reactor for carbon dioxide methanation, Chem. Eng. J. 313 (2017) 847–857, https://doi.org/10.1016/j.cej.2016.10.131.

[35] Z. Bian, H. Xia, W. Zhong, B. Jiang, Y. Yu, Z. Wang, K. Yu, CFD simulation on hydrogen-membrane reactor integrating cyclohexane dehydrogenation and CO_2 methanation reactions: A conceptual study, Energy Convers. Manag 235 (2021), 113989, https://doi.org/10.1016/j.enconman.2021.113989.

[36] S. Pérez, E. Del Molino, V.L. Barrio, Modeling and Testing of a Milli-Structured Reactor for Carbon Dioxide Methanation, Int. J. Chem. React. Eng. 15 (2019), 20180238, https://doi.org/10.1515/ijcre-2018-0238.

[37] S. Ich Ngo, Y. Il Lim, D. Lee, M. Won Seo, S. Kim, Experiment and numerical analysis of catalytic CO_2 methanation in bubbling fluidized bed reactor, Energy Convers. Manag 233 (2021), 113863, https://doi.org/10.1016/j.enconman.2021.113863.

[38] A. Di Nardo, G. Calchetti, C. Bassano, P. Deiana, CO_2 methanation in a shell and tube reactor CFD simulations: High temperatures mitigation analysis, Chem. Eng. Sci. 246 (2021), 116871, https://doi.org/10.1016/j.ces.2021.116871.

[39] W. Zhang, H. Machida, H. Takano, K. Izumiya, K. Norinaga, Computational fluid dynamics simulation of CO_2 methanation in a shell-and-tube reactor with multi-region conjugate heat transfer, Chem. Eng. Sci. 211 (2020), 115276, https://doi.org/10.1016/j.ces.2019.115276.

[40] V. Chandraker, G. Paramasivan, A.J. Chandy, Computational investigations of enrichment effects for CO_2 methanation in Sabatier microchannel reactors, Chem. Eng. Res. Des. 182 (2022) 51–65, https://doi.org/10.1016/j.cherd.2022.03.035.

[41] C. Choi, A. Khuenpetch, W. Zhang, S. Yasuda, Y. Lin, H. Machida, H. Takano, K. Izumiya, Y. Kawajiri, K. Norinaga, Determination of Kinetic Parameters for CO_2 Methanation (Sabatier Reaction) over Ni/ZrO_2 at a Stoichiometric Feed-Gas Composition under Elevated Pressure, Energy Fuels 35 (2021) 91–112, https://doi.org/10.1021/acs.energyfuels.1c01534.

[42] J. Xu, G.F. Froment, Methane steam reforming, methanation and water-gas shift: I. Intrinsic kinetics, AIChE J. 35 (1989) 88–96, https://doi.org/10.1002/aic.690350109.

[43] I. Champon, A. Bengaouer, A. Chaise, S. Thomas, A.C. Roger, Carbon dioxide methanation kinetic model on a commercial Ni/Al_2O_3 catalyst, J. CO_2 Util. 34 (2019) 256–265, https://doi.org/10.1016/j.jcou.2019.05.030.

[44] G. Soave, Equilibrium constants from a modified Redlich-Kwong equation of state, Chem. Eng. Sci. 27 (1972) 1197–1203, https://doi.org/10.1016/0009-2509(72)80096-4.

[45] M. Zamudio, C.E. Schwarz, J.H. Knoetze, Experimental measurement and modelling with Aspen Plus® of the phase behaviour of supercritical CO2 + (n-dodecane + 1-decanol + 3,7-dimethyl-1-octanol), J. Supercrit. Fluids 84 (2013) 132–145, https://doi.org/10.1016/j.supflu.2013.09.015.

[46] D. Peng, D.B. Robinson, A new two-constant equation of state, Ind. Eng. Chem. Fundam. 15 (1976) 59–64, https://doi.org/10.1021/i160057a011.

[47] H.S. Fogler. Elements of Chemical Reaction Engineering, sixth ed...., Pearson, London, 2020.

[48] A.M. D'Angelo, A.L. Chaffee, Correlations between oxygen uptake and vacancy concentration in Pr-doped CeO_2, ACS Omega 2 (2017) 2544–2551, https://doi.org/10.1021/acsomega.7b00550.

[49] V. Alcalde-Santiago, A. Davó-Quiñonero, D. Lozano-Castelló, A. Quindimil, U. De-La-Torre, B. Pereda-Ayo, J.A. González-Marcos, J.R. González-Velasco, A. Bueno-López, Ni/LnO_x catalysts (Ln═La, Ce or Pr) for CO_2 Methanation, ChemCatChem 11 (2019) 810–819, https://doi.org/10.1002/cctc.201801585.

[50] K. Bourikas, J. Stavropoulos, C.S. Garoufalis, C. Kordulis, T. Petsi, A. Lycourghiotis, Interfacial impregnation chemistry in the synthesis of nickel catalysts supported on titania, Chem. - A Eur. J. 17 (2011) 1201–1213, https://doi.org/10.1002/chem.201001370.

[51] M.A. Małecka, L. Kepiński, W. Miśta, Structure evolution of nanocrystalline CeO_2 and $CeLnO_x$ mixed oxides (Ln = Pr, Tb, Lu) in O_2 and H_2 atmosphere and their catalytic activity in soot combustion, Appl. Catal. B Environ. 74 (2007) 290–298, https://doi.org/10.1016/j.apcatb.2007.02.021.

[52] M. Thommes, K. Kaneko, A.V. Neimark, J.P. Olivier, F. Rodriguez-Reinoso, J. Rouquerol, K.S.W. Sing, Physisorption of gases, with special reference to the evaluation of surface area and pore size distribution (IUPAC Technical Report), Pure Appl. Chem. 87 (2015) 1051–1069, https://doi.org/10.1515/pac-2014-1117.

[53] J.R.A. Sietsma, J.D. Meeldijk, M. Versluijs-Helder, A. Broersma, A. Jos Van Dillen, P.E. De Jongh, K.P.De Jong, Ordered mesoporous silica to study the preparation of Ni/SiO_2 ex nitrate catalysts: Impregnation, drying, and thermal treatments, Chem. Mater. 20 (2008) 2921–2931, https://doi.org/10.1021/cm702610h.

[54] B. Li, X. Yuan, B. Li, X. Wang, Impact of pore structure on hydroxyapatite supported nickel catalysts (Ni/HAP) for dry reforming of methane, Fuel Process. Technol. 202 (2020), 106359, https://doi.org/10.1016/j.fuproc.2020.106359.

[55] J. Cai, Y. Han, S. Chen, E.J. Crumlin, B. Yang, Y. Li, Z. Liu, CO_2 Activation on Ni (111) and Ni(100) Surfaces in the Presence of H_2O: An Ambient-Pressure X-ray Photoelectron Spectroscopy Study, J. Phys. Chem. C. 123 (2019) 12176–12182, https://doi.org/10.1021/acs.jpcc.8b11698.

[56] Y. Ma, J. Liu, M. Chu, J. Yue, Y. Cui, G. Xu, Enhanced low-temperature activity of CO_2 methanation over Ni/CeO_2 catalyst, Catal. Lett. 152 (2022) 872–882, https://doi.org/10.1007/s10562-021-03677-7.

[57] K. Liu, X. Xu, J. Xu, X. Fang, L. Liu, X. Wang, The distributions of alkaline earth metal oxides and their promotional effects on Ni/CeO_2 for CO_2 methanation, J. CO_2 Util. 38 (2020) 113–124, https://doi.org/10.1016/j.jcou.2020.01.016.

[58] M.M. Makri, M.A. Vasiliades, K.C. Petallidou, A.M. Efstathiou, Effect of support composition on the origin and reactivity of carbon formed during dry reforming of methane over 5 wt% Ni/$Ce_{1-x}M_xO_{2-\delta}$ (M = Zr^{4+}, Pr^{3+}) catalysts, Catal. Today 259 (2016) 150–164, https://doi.org/10.1016/j.cattod.2015.06.010.

[59] C.M. Damaskinos, M.A. Vasiliades, A.M. Efstathiou, The effect of Ti^{4+} dopant in the 5 wt% Ni/$Ce_{1-x}Ti_xO_{2-\delta}$ catalyst on the carbon pathways of dry reforming of methane studied by various transient and isotopic techniques, Appl. Catal. A Gen. 579 (2019) 116–129, https://doi.org/10.1016/j.apcata.2019.04.023.

[60] M. Li, H. Amari, A.C. van Veen, Metal-oxide interaction enhanced CO_2 activation in methanation over ceria supported nickel nanocrystallites, Appl. Catal. B Environ. 239 (2018) 27–35, https://doi.org/10.1016/j.apcatb.2018.07.074.

[61] J. Yang, S. Hu, Y. Fang, S. Hoang, L. Li, W. Yang, Z. Liang, J. Wu, J. Hu, W. Xiao, C. Pan, Z. Luo, J. Ding, L. Zhang, Y. Guo, Oxygen vacancy promoted O_2 activation over perovskite oxide for low-temperature CO oxidation, ACS Catal. 9 (2019) 9751–9763, https://doi.org/10.1021/acscatal.9b02408.

[62] S. Lu, F. Wang, C. Chen, F. Huang, K. Li, Catalytic oxidation of formaldehyde over CeO_2-Co_3O_4 catalysts, J. Rare Earths 35 (2017) 867–874, https://doi.org/10.1016/S1002-0721(17)60988-8.

[63] A.I. Tsiotsias, B. Ehrhardt, B. Rudolph, L. Nodari, S. Kim, W. Jung, N.D. Charisiou, M.A. Goula, S. Mascotto, Bimetallic exsolved heterostructures of controlled composition with tunable catalytic properties, ACS Nano 16 (2022) 8904–8916, https://doi.org/10.1021/acsnano.1c11111.

[64] H. Borchert, Y.V. Frolova, V.V. Kaichev, I.P. Prosvirin, G.M. Alikina, A. I. Lukashevich, V.I. Zaikovskii, E.M. Moroz, S.N. Trukhan, V.P. Ivanov, E. A. Paukshtis, V.I. Bukhtiyarov, V.A. Sadykov, Electronic and chemical properties of nanostructured cerium dioxide doped with praseodymium, J. Phys. Chem. B 109 (2005) 5728–5738, https://doi.org/10.1021/jp045828c.

[65] K.N. Papageridis, N.D. Charisiou, S.L. Douvartzides, V. Sebastian, S.J. Hinder, M. A. Baker, S. AlKhoori, K. Polychronopoulou, M.A. Goula, Effect of operating parameters on the selective catalytic deoxygenation of palm oil to produce renewable diesel over Ni supported on Al_2O_3, ZrO_2 and SiO_2 catalysts, Fuel Process. Technol. 209 (2020), 106547, https://doi.org/10.1016/j.fuproc.2020.106547.

[66] N.D. Charisiou, G. Siakavelas, L. Tzounis, B. Dou, V. Sebastian, S.J. Hinder, M. A. Baker, K. Polychronopoulou, M.A. Goula, Ni/Y_2O_3–ZrO_2 catalyst for hydrogen production through the glycerol steam reforming reaction, Int. J. Hydrog. Energy 45 (2020) 10442–10460, https://doi.org/10.1016/j.ijhydene.2019.04.237.

[67] M.C. Biesinger, B.P. Payne, A.P. Grosvenor, L.W.M. Lau, A.R. Gerson, R.S.C. Smart, Resolving surface chemical states in XPS analysis of first row transition metals, oxides and hydroxides: Cr, Mn, Fe, Co and Ni, Appl. Surf. Sci. 257 (2011) 2717–2730, https://doi.org/10.1016/j.apsusc.2010.10.051.

[68] X. Zhang, L. Liu, J. Feng, X. Ju, J. Wang, T. He, P. Chen, Ru Nanoparticles on Pr_2O_3 as an Efficient Catalyst for Hydrogen Production from Ammonia Decomposition, Catal. Lett. 152 (2021) 1170–1181, https://doi.org/10.1007/s10562-021-03709-2.

[69] S.L. Rodríguez, A. Davó-Quiñonero, J. Juan-Juan, E. Bailón-García, D. Lozano-Castelló, A. Bueno-López, Effect of Pr in CO_2 Methanation Ru/CeO_2 Catalysts, J. Phys. Chem. C. 125 (2021) 12038–12049, https://doi.org/10.1021/acs.jpcc.1c03539.

[70] B.E. Kayaalp, Y.J. Lee, A. Kornowski, S. Gross, M. D'Arienzo, S. Mascotto, Cooperative assembly synthesis of mesoporous $SrTiO_3$ with enhanced photocatalytic properties, RSC Adv. 6 (2016) 90401–90409, https://doi.org/10.1039/c6ra13800d.

[71] J. Scholz, A. Garbujo, B. Kayaalp, K. Klauke, A. Glisenti, S. Mascotto, Functional nanostructured perovskite oxides from radical polymer precursors, Inorg. Chem. 58 (2019) 15942–15952, https://doi.org/10.1021/acs.inorgchem.9b02460.

[72] G. Varvoutis, M. Lykaki, S. Stefa, V. Binas, G.E. Marnellos, M. Konsolakis, Deciphering the role of Ni particle size and nickel-ceria interfacial perimeter in the low-temperature CO_2 methanation reaction over remarkably active Ni/CeO_2 nanorods, Appl. Catal. B Environ. 297 (2021), 120401, https://doi.org/10.1016/j.apcatb.2021.120401.

[73] S. Farsi, W. Olbrich, P. Pfeifer, R. Dittmeyer, A consecutive methanation scheme for conversion of CO_2 – A study on Ni_3Fe catalyst in a short-contact time micro packed bed reactor, Chem. Eng. J. 388 (2020), 124233, https://doi.org/10.1016/j.cej.2020.124233.

[74] S. Lin, Z. Hao, J. Shen, X. Chang, S. Huang, M. Li, X. Ma, Enhancing the CO_2 methanation activity of Ni/CeO_2 via activation treatment-determined metal-support interaction, J. Energy Chem. 59 (2021) 334–342, https://doi.org/10.1016/j.jechem.2020.11.011.

[75] Z. Bian, Y.M. Chan, Y. Yu, S. Kawi, Morphology dependence of catalytic properties of Ni/CeO_2 for CO_2 methanation: A kinetic and mechanism study, Catal. Today 347 (2020) 31–38, https://doi.org/10.1016/j.cattod.2018.04.067.

[76] I. Luisetto, S. Stendardo, S.M. Senthil Kumar, K. Selvakumar, J.K. Kesavan, G. Iucci, U. Pasqual Laverdura, S. Tuti, One-pot synthesis of $Ni_{0.05}Ce_{0.95}O_{2-\delta}$ catalysts with nanocubes and nanorods morphology for CO_2 methanation reaction and in operando drift analysis of intermediate species, Processes 9 (2021) 1899, https://doi.org/10.3390/pr9111899.

[77] G. Garbarino, C. Wang, T. Cavattoni, E. Finocchio, P. Riani, M. Flytzani-Stephanopoulos, G. Busca, A study of Ni/La-Al_2O_3 catalysts: A competitive system for CO_2 methanation, Appl. Catal. B Environ. 248 (2019) 286–297, https://doi.org/10.1016/j.apcatb.2018.12.063.